

1 **A multi-dimensional spectral description of ocean variability**

2 CIMARRON WORTHAM \*

*Department of Earth, Atmospheric and Planetary Sciences, Massachusetts Institute of Technology,*

*Cambridge, Massachusetts*

3 CARL WUNSCH

*Department of Earth and Planetary Sciences, Harvard University, Cambridge, Massachusetts,*

---

\* *Corresponding author address:* Cimarron Wortham, Department of Earth, Atmospheric and Planetary Sciences, Massachusetts Institute of Technology, 77 Massachusetts Ave., Cambridge, MA 02139.

E-mail: worthamc@mit.edu

## ABSTRACT

4  
5 An updated empirical, analytical model for the frequency and wavenumber distribution of  
6 balanced motion in the ocean is presented. The spectrum-model spans periods longer than  
7 the inertial but shorter than a decade, and wavelengths between 100 km and 10,000 km. As-  
8 suming geostrophic dynamics, a spectrum-model for the streamfunction is constructed to be  
9 consistent with a range of observations, including sea surface height from satellite altimetry,  
10 velocity from moored and shipboard instruments, and temperature from moorings. First  
11 order characteristics of the observed spectra, including amplitude and spectral moments,  
12 vary slowly geographically. The spectrum-model is horizontally anisotropic, accommodating  
13 observations that zonal wavenumber-frequency spectra are dominated by a “nondispersive  
14 line”. Qualitative and quantitative agreement is found with one-dimensional frequency and  
15 wavenumber spectra, and observed vertical profiles of variance. Illustrative application is  
16 made of the model spectrum to observing system design, data mapping, and uncertainty  
17 estimation for trends.

# 1. Introduction

Data describing the general circulation of the ocean are extremely noisy (e.g., Ganachaud (2003); Zhai et al. (2011)). Extraction of signals from such observations requires a detailed knowledge of the space and time-scales of the stochastic variability. Of course, one person's noise is another's signal. Stochastic variability is itself a part of the ocean circulation and is of great interest in its own right. Since the time of the Mid-Ocean Dynamics Experiment (MODE Group 1978), the oceanographic community has collected countless measurements showing variability of different types (including velocity, temperature, surface elevation) in time and/or space. Synthesizing those observations of ocean variability into a quantitatively useful form is a considerable challenge. The specific availability since 1992 of high accuracy near-global altimetry has sparked a number of partial synthesis efforts, including estimates of the frequency spectrum (e.g., Le Traon (1990); Lin et al. (2008); Hughes and Williams (2010)) and of wavenumber spectra (e.g., Stammer (1997); Le Traon et al. (2008); Xu and Fu (2012)). A first attempt at the desired combined frequency/wavenumber spectrum was made by Zang and Wunsch (2001) and Wunsch (2010).

The purpose of this present paper is to extend these earlier efforts so as to construct a full four-dimensional (three wavenumbers plus frequency) spectral representation of oceanic variability, along with an estimate of the extent to which it is likely both accurate and useful. A wide range of observations are used, including sea surface height (SSH) from altimetry, temperature and velocity time series from moored instruments, and velocity from shipboard current meters. As a consequence of the available observational record, the resulting description extends from periods longer than the inertial to about a decade, and wavelengths from about 100 km to several thousands of kilometers. As a short-hand, variability in these ranges will be referred to as “balanced motions”, suggesting the expectation of near-geostrophy in their physics.

Altimetric data provide the only continuous, near-global record of ocean variability with a simple dynamical interpretation. (Owing to the complex boundary layers at the air-sea

45 interface, sea surface temperature, salinity, and color are much more difficult to interpret.)  
46 As such, the altimetric record provides the backbone of the resulting spectral model, jointly  
47 covering horizontal wavenumber and frequency.

48 Like all data, the altimetric record contains complicated structures from measurement  
49 noise and from the elaborate data processing involved in estimating SSH from the raw  
50 observations. Accounting for these complexities has to be part of the synthesis effort. The  
51 greatest problem with reliance on SSH is in understanding how it reflects motions interior  
52 to the ocean. Although in the geostrophic limit employed here, boundary layer phenomena  
53 are not of first-order concern, the partition of SSH into barotropic and baroclinic structures,  
54 expected to be a function of wavenumber/frequency and geography, is perhaps the greatest  
55 theoretical and observational challenge.

56 To address the problem, the vertical structure of variability is inferred where possible  
57 from moored instruments. Unfortunately, the number of moored instruments with sufficient  
58 duration and vertical resolving power is very limited (Scott et al. 2010). What data are  
59 available are used in combination with basic theoretical ideas to construct a strawman spec-  
60 trum. Some of the theoretical considerations are put in context by employing an oceanic  
61 general circulation model (GCM; called ECCO2), with the strong caveat that the same very  
62 small data base renders nearly impossible tests of model skill.

63 To a degree, this paper attempts to do for oceanic balanced motions what the Garrett-  
64 Munk (Garrett and Munk 1972, 1975) spectrum did for the internal wave band. Their  
65 work has served as a tool for interpreting experimental results, highlighted gaps in the  
66 observational record, and inspired theoretical efforts to explain their description. At the end  
67 of this paper, the utility of the present spectrum-model<sup>1</sup> will be demonstrated by application  
68 to the important problem of oceanic trend determination. Importantly, the spectrum-model  
69 can be used to predict vertical and horizontal coherence between measurements. Many

---

<sup>1</sup>The terminology “spectrum-model” is used to distinguish the results from a “spectral model” (GCM formulated in spectral space) or “model spectrum” (spectrum of GCM output).

70 elements of the result are also in need of theoretical explanation, and perhaps progress in  
 71 that direction will be a result.

## 72 2. Dynamic model for balanced motion

73 Zang (2000) took the linearized, quasi-geostrophic,  $\beta$ -plane equations as a basic dynam-  
 74 ical model and showed that the spectra of horizontal velocity  $(u, v)$ , vertical velocity  $w$ ,  
 75 vertical displacement  $\zeta$ , density  $\rho$ , potential temperature  $\theta$ , and pressure  $p$  can all be derived  
 76 from the spectrum of the geostrophic streamfunction  $\psi = p/\rho_0 f_0$ , where  $\rho_0$  is the reference  
 77 density and  $f_0$  is the local Coriolis parameter. In this section, the basic dynamical model  
 78 introduced by Zang (2000) is reviewed and the implied relations between observable spectra  
 79 are recorded. Separating variables,

$$\psi(x, y, z, t) = \sum_{n=0}^{\infty} \psi_n(x, y, z, t) \quad (1)$$

$$= \sum_{n=0}^{\infty} \Psi_n(x, y, t) F_n(z), \quad (2)$$

80 where the orthonormal vertical modes,  $F_n(z)$ , satisfy (e.g., Gill 1982)

$$\frac{d}{dz} \left( \frac{f_0^2}{N^2(z)} \frac{dF}{dz} \right) + \gamma^2 F(z) = 0, \quad (3)$$

81 where  $N(z)$  is the buoyancy frequency. With its boundary conditions (3) forms a Sturm-  
 82 Liouville eigenvalue problem whose eigenfunctions,  $F_n(z)$ ,  $0 \leq n < \infty$ , represent the vertical  
 83 structure of horizontal velocity free modes in the ocean, and whose eigenvalues are related  
 84 to the deformation radius  $L_d = 1/\gamma$ .

85 The vertical velocity is proportional to another vertical mode,  $G_n(z)$ :

$$G_n(z) = \frac{1}{N^2(z)} \frac{dF_n(z)}{dz}, \quad (4)$$

86 satisfying

$$\frac{d^2 G_n(z)}{dz^2} + \gamma_n^2 \frac{N^2(z)}{f_0^2} G_n(z) = 0 \quad (5)$$

87 with appropriate boundary conditions.

88 Equations (3) and (4) are typically derived under the “basic textbook theory” (BTT)  
 89 assumptions of linearity, resting mean state, and flat bottom and rigid-lid boundary condi-  
 90 tions. Although these conditions are not satisfied in the real ocean, solutions to (3) form  
 91 a complete set capable of describing any vertical structure. However, if the assumptions  
 92 are violated, the representation may be very inefficient. Alternative surface boundary con-  
 93 ditions account for Ekman pumping (Philander 1978) or nonlinear buoyancy advection, as  
 94 in “surface quasi-geostrophic” (SQG) theory (Lapeyre and Klein 2006). Alternative bottom  
 95 boundary conditions account for bathymetry (Tailleux and McWilliams 2001; Killworth and  
 96 Blundell 2004). Important modifications to (3) will be discussed in section 5.

97 Treating the streamfunction as a sum of plane waves, the full streamfunction in mode  $n$   
 98 is

$$\psi_n(x, y, z, t) = \int_0^\infty \int_{-\infty}^\infty \int_{-\infty}^\infty \tilde{\psi}(k, l, \omega, n) F_n(z) e^{i2\pi(kx+ly-\omega t)} dk dl d\omega, \quad (6)$$

99 where  $\tilde{\psi}(k, l, \omega, n)$  is the Fourier transform of the streamfunction. Note that cyclic frequencies  
 100 and wavenumbers are being used. For a generic variable  $\chi_n(x, y, z, t)$ , the  $n^{\text{th}}$  mode is

$$\chi_n(x, y, z, t) = \int_0^\infty \int_{-\infty}^\infty \int_{-\infty}^\infty \tilde{\chi}(k, l, \omega, z, n) \tilde{\psi}(k, l, \omega, n) e^{i2\pi(kx+ly-\omega t)} dk dl d\omega. \quad (7)$$

101 Zang and Wunsch (2001) derived the characteristic functions  $\tilde{\chi}(k, l, \omega, z, n)$ , and the repre-  
 102 sentations are:

$$\tilde{p}(k, l, \omega, z, n) = \rho_0 f_0 F_n(z), \quad (8)$$

$$\tilde{u}(k, l, \omega, z, n) = -i2\pi l F_n(z), \quad (9)$$

$$\tilde{v}(k, l, \omega, z, n) = i2\pi k F_n(z), \quad (10)$$

$$\tilde{w}(k, l, \omega, z, n) = i2\pi \omega f_0 G_n(z), \quad (11)$$

$$\tilde{\rho}(k, l, \omega, z, n) = -\frac{\rho_0 f_0}{g} N^2(z) G_n(z), \quad (12)$$

$$\tilde{\zeta}(k, l, \omega, z, n) = -f_0 G_n(z), \quad (13)$$

$$\tilde{\theta}(k, l, \omega, z, n) = f_0 \frac{\partial \theta_0}{\partial z} G_n(z), \quad (14)$$

103 where  $\theta_0$  is the time-mean potential temperature.

104 Different frequencies, wavenumbers, and vertical modes are assumed uncorrelated as-  
105 suring horizontal spatial and temporal stationarity. Among other phenomena, these as-  
106 sumptions ignore the possible presence of coherent mesoscale features (Chelton et al. 2011).  
107 Because they are represented by phase-locked modes, an increased variance is expected rela-  
108 tive to that of a stationary random wave field. While Chelton et al. (2011) show the presence  
109 of coherent features in the SSH record, other forms of variability are also plainly present in  
110 the records. A more complete description than the one to be obtained here eventually needs  
111 to account for both coherent and incoherent (statistically stationary, random) components  
112 of the variability.

### 113 *A spectrum-model*

114 The three-dimensional frequency and wavenumber spectrum for the mode  $n$  streamfunc-  
115 tion is

$$\Phi_\psi(k, l, \omega, n) = \langle |\tilde{\psi}(k, l, \omega, n)|^2 \rangle, \quad (15)$$

116 where angle brackets represent an ensemble average. For other variables, the spectrum at  
117 depth  $z$  and mode  $n$  can be calculated from the spectrum of the streamfunction and the  
118 appropriate characteristic function:

$$\Phi_\chi(k, l, \omega, z, n) = |\tilde{\chi}(k, l, \omega, z, n)|^2 \Phi_\psi(k, l, \omega, n) \quad (16)$$

119 and which can be summed over all vertical modes:

$$\Phi_\chi(k, l, \omega, z) = \sum_{n=0}^{\infty} |\tilde{\chi}(k, l, \omega, z, n)|^2 \Phi_\psi(k, l, \omega, n). \quad (17)$$

120 Two- or one-dimensional spectra can be obtained by integrating the three-dimensional  
121 spectrum over one or two dimensions. Notation for the one-, two-, or three-dimensional  
122 spectra of a variable  $\chi$  can be quite cumbersome.  $\Phi_\chi(k, l, \omega, z)$  is written for the spectrum  
123 of  $\chi$  at depth  $z$ , and the arguments  $(k, l, \omega)$  denote the dimensionality. For example, the

124 two-dimensional wavenumber spectrum is

$$\Phi_\chi(k, l, z) = \int_0^\infty \Phi_\chi(k, l, \omega, z) d\omega. \quad (18)$$

125 Similarly,

$$\Phi_\chi(l, z) = \int_0^\infty \int_{-\infty}^\infty \Phi_\chi(k, l, \omega, z) dk d\omega. \quad (19)$$

126 For simplicity and in the absence of observational evidence to the contrary (Zang and  
127 Wunsch 2001), we assume that the shape of the spectrum in horizontal wavenumber-frequency  
128 space is independent of mode number. Accordingly, a streamfunction spectrum of the form

$$\Phi_\psi(k, l, \omega, n; \phi, \lambda) = \Phi_\psi(k, l, \omega; \phi, \lambda) E(n) I(\phi, \lambda) \quad (20)$$

129 is proposed, where  $\Phi_\psi(k, l, \omega; \phi, \lambda)$  is the three-dimensional wavenumber-frequency spectrum,  
130 and which changes slowly with latitude  $\phi$  and longitude  $\lambda$ .  $E(n)$  represents the relative  
131 contribution from each vertical mode  $n$ .  $I(\phi, \lambda)$  is a normalization factor:

$$I(\phi, \lambda) = \text{EKE} \left[ \int_0^\infty \int_{-\infty}^\infty \int_{-\infty}^\infty \frac{1}{2} (|\tilde{u}|^2 + |\tilde{v}|^2) \Phi_\psi(k, l, \omega; \phi, \lambda) dk dl d\omega \sum_{n=0}^\infty E(n) \right]^{-1}, \quad (21)$$

132 where EKE is the the surface eddy kinetic energy estimated from altimetry (Stammer 1997).  
133 With this normalization, (20) matches the observed surface eddy kinetic energy.

134 Many applications of the spectrum-model rely on the Wiener-Khinchin theorem, show-  
135 ing that the Fourier transform of the stationary process power spectrum is the covariance  
136 function:

$$\text{Cov}(r_x, r_y, \tau) = \int_0^\infty \int_{-\infty}^\infty \int_{-\infty}^\infty \Phi_\chi(k, l, \omega) e^{i2\pi(kr_x + lr_y + \omega\tau)} dk dl d\omega, \quad (22)$$

137 where  $r_x$ ,  $r_y$ ,  $\tau$  are the displacements in the zonal, meridional, and temporal directions,  
138 respectively. Normalizing by the signal variance gives the correlation function

$$\text{Cor}(r_x, r_y, \tau) = \frac{\text{Cov}(r_x, r_y, \tau)}{\sigma_\chi^2}, \quad (23)$$

139 where  $\sigma_\chi^2$  is the variance of  $\chi$ . For standard one-dimensional autocovariances,

$$\text{Cov}(r_x) = \int_0^\infty \int_{-\infty}^\infty \int_{-\infty}^\infty \Phi_\chi(k, l, \omega) e^{i2\pi kr_x} dk dl d\omega. \quad (24)$$



140 For two time series (possibly representing different quantities) at locations  $(x, y, z)$  and  
 141  $(x + r_x, y + r_y, z')$ , the cross-spectrum between  $\chi(x, y, z, t)$  and  $\Upsilon(x + r_x, y + r_y, z', t)$  is

$$\Phi_{\chi\Upsilon}(\omega; r_x, r_y, z, z') = \sum_{n=0}^{\infty} \int_{-\infty}^{\infty} \int_{-\infty}^{\infty} \tilde{\chi}(k, l, \omega, z, n) \tilde{\Upsilon}^*(k, l, \omega, z', n) \Phi_{\psi}(k, l, \omega, n) e^{i2\pi(kr_x + lr_y)} dk dl, \quad (26)$$

142 where  $\tilde{\chi}$  and  $\tilde{\Upsilon}$  are the characteristic functions for the two variables and \* indicates the  
 143 complex conjugate. The coherence is

$$Coh(\omega; r_x, r_y, z, z') = \frac{\Phi_{\chi\Upsilon}(\omega; r_x, r_y, z, z')}{\sqrt{\Phi_{\chi}(\omega, z) \Phi_{\Upsilon}(\omega, z')}}. \quad (27)$$

144 Spatial variation in the spectral shape is neglected in the coherence calculation. Observations  
 145 out to periods of a few years show little correlation between measurements separated by  
 146 more than a few hundred kilometers (Stammer 1997). While significant coherence over long  
 147 distances may exist at very low frequencies (due, for example, to a shift in gyre location over  
 148 decades), we are not aware of any supporting observations.

### 149 3. Observed spectrum

150 From the earlier work cited above, it is clear from the outset that, unlike the internal  
 151 wave case, a truly universal spectral description of balanced motions is impossible. Many  
 152 qualitative aspects of the spectrum vary geographically including eddy kinetic energy levels,  
 153 which change by over four orders of magnitude (Stammer 1997). The slowly varying geo-  
 154 graphical factors attempt to accommodate this spatial nonstationarity in as simple a fashion  
 155 as possible.

156 Oceanic spectra, grouped by data type, are now examined.

## 158 1) MULTI-DIMENSIONAL SPECTRAL SHAPE

159 The most complete observations of the spectrum of ocean variability come from the  
160 AVISO multi-mission mapped altimetry product (Ducet et al. 2000). We use the “reference”  
161 version, in which data from two simultaneous satellite altimeter missions were merged and  
162 mapped onto a  $1/3^\circ$  Mercator grid at 7-day intervals for the period October 1992–December  
163 2010; the 1993–1999 mean was removed at each grid point. From the AVISO product, the  
164 three-dimensional power spectrum can be estimated as discussed in Wortham (2013).

165 One striking characteristic of the resulting spectrum is its dominance almost everywhere  
166 by a “nondispersive” straight line in zonal wavenumber-frequency space (Wunsch 2009, 2010;  
167 Ferrari and Wunsch 2010; Early et al. 2011) with phase speed independent of wavelength or  
168 frequency over a wide range. This phase speed is faster than the standard long Rossby wave  
169 prediction at most latitudes (Chelton and Schlax 1996) and has attracted wide theoretical  
170 attention. The nondispersive line dominates at wavelengths larger than about 500 km, and  
171 periods longer than two weeks at  $10^\circ$ , or longer than two months at  $40^\circ$ . At shorter wave-  
172 lengths, the anisotropy diminishes, and the spectrum appears to approach an isotropic power  
173 law in wavenumber, though the resolution of the gridded altimetry product is insufficient  
174 to make a definitive statement at wavelengths shorter than 200 km. At high frequency, the  
175 spectrum approaches approximate power laws in both frequency and wavenumber.

## 176 2) DOMINANT PERIODS AND WAVELENGTHS

177 Display and interpretation of multi-dimensional spectral structures is extremely chal-  
178 lenging and some simplified representations are useful. For example, Jacobs et al. (2001)  
179 estimated zonal wavelength, meridional wavelength, and period by fitting an exponential to  
180 the binned covariance function estimated from altimetry. Here, spectral moments (Vanmar-

181 cke 2010) are used. Define,

$$\langle \omega^q \rangle = \int_0^\infty \omega^q \Phi_\eta(\omega) d\omega / \int_0^\infty \Phi_\eta(\omega) d\omega, \quad (28)$$

$$\langle k^q \rangle = \int_0^\infty k^q [\Phi_\eta(k) + \Phi_\eta(-k)] dk / \int_0^\infty [\Phi_\eta(k) + \Phi_\eta(-k)] dk, \quad (29)$$

$$\langle l^q \rangle = \int_0^\infty l^q [\Phi_\eta(l) + \Phi_\eta(-l)] dl / \int_0^\infty [\Phi_\eta(l) + \Phi_\eta(-l)] dl, \quad (30)$$

182 for integer  $q$ . For  $k$  and  $l$ , the moments of the spectrum are averaged over both positive and  
 183 negative wavenumber<sup>2</sup> and are estimated globally on a 5° grid as follows: for each point, using  
 184 SSH maps within a box 10° in longitude by 30° latitude, the spatial mean and linear trend  
 185 in latitude and longitude are removed at each time step, and the three-dimensional FFT is  
 186 computed for the region.  $k$ - $l$ - $\omega$  spectra are computed from the FFT, averaged over three  
 187 neighboring frequency/wavenumber bands. Other windowing functions did not significantly  
 188 alter the results. See Wortham (2013) for further details.

189 Maps of the inverse of the first moments of frequency and wavenumber are shown (Fig. 1).  
 190 Hatched areas in the wavelength plots indicate regions where more power lies in the posi-  
 191 tive wavenumber part of the spectrum than in the negative wavenumber part. For zonal  
 192 wavenumber, hatching indicates a dominance of eastward propagation. For meridional  
 193 wavenumber, hatching indicates a dominance of poleward propagation. Dominant peri-  
 194 ods increase from less than 100 days near the equator to about 300 days at 40°. Dominant  
 195 zonal wavelengths decrease from about 1400 km near the equator to 750 km at 40°, while  
 196 meridional wavelengths range from 900 km to 650 km. Such maps provide a quantitative  
 197 point of comparison for the spectrum-model in section 4.

198 The AVISO mapping procedure imposes space and time correlation scales on the data  
 199 product (Ducet et al. 2000), which impact estimated dominant periods and wavelengths.  
 200 Specifically, AVISO frequency spectra have a steeper high-frequency roll-off than other ob-  
 201 servations, resulting in longer dominant periods (Chiswell and Rickard 2008). Despite such

---

<sup>2</sup>Alternatively, we might calculate the moments for positive and negative wavenumber independently, as  
 in Wunsch (2010).

202 limitations, the AVISO gridded altimetry is used since it allows for straightforward compu-  
203 tation of zonal and meridional spectra.

### 204 3) SPECTRAL SLOPES

205 While the gridded altimetry provides a useful tool for studying the three-dimensional SSH  
206 spectrum and its global variations, the AVISO mapping procedure significantly alters the  
207 shape of the resulting spectrum (Wortham 2013). Therefore, we now consider the spectrum  
208 from TOPEX/POSEIDON along-track altimetry, rather than the gridded altimetry product,  
209 using the multitaper estimate as with all one-dimensional records in this paper.

210 Observed wavenumber spectra are shown for two locations in the North Pacific (Fig. 2):  
211 a high energy region of the Kuroshio extension centered at 35°N, 168°E and a relatively low  
212 energy region of the subtropical gyre centered at 35°N, 222°E. In the high energy region, the  
213 spectral slope in the 100–200 km wavelength band is close to  $k^{-4}$ , while the spectral slope  
214 is significantly flatter in the low energy region, closer to  $k^{-2}$ . In the high wavenumber tails,  
215 the spectrum flattens to  $k^{-1}$  at both locations. For reference, we also show the wavenum-  
216 ber spectrum from AVISO gridded altimetry, linearly interpolated along the satellite track.  
217 The spectrum from AVISO gridded altimetry is steeper than from un-gridded altimetry at  
218 wavelengths shorter than about 250 km.

219 Wunsch and Stammer (1995), Le Traon et al. (2008), and Xu and Fu (2012) have fit  
220 power laws to the high-wavenumber SSH spectrum. High-wavenumber spectral slopes vary  
221 geographically, but the true values remain uncertain. Much of the high wavenumber tail is  
222 due to noise, but the extent to which the altimetric wavenumber spectrum is contaminated  
223 by noise is a matter of debate. Stammer (1997) concluded, based on filtered along-track  
224 wavenumber spectra from altimetry, that SSH spectra displayed a remarkably universal  $k^{-4}$   
225 power law at wavelengths shorter than 400 km. Xu and Fu (2012) estimated spectral slopes  
226 varying from  $k^{-4.5}$  in high energy regions to  $k^{-2}$  in low energy subtropics, and  $k^{-1}$  in the  
227 tropics.

228 For SSH frequency spectral slopes, Stammer (1997) found that different regions (tropical,  
229 high, and low energy) behaved differently in the low frequency limit, but all approached an  
230  $\omega^{-2}$  power law at around 30 day periods. The frequency spectrum of sea surface slope  
231 (proportional to velocity) was found to have an almost white long-period plateau,  $\omega^{-1/2}$   
232 power-law relation for periods between 40 and 250 days, and roughly a  $\omega^{-2}$  relation on  
233 shorter periods. However, the Nyquist period of the altimetric data is about 20 days, so  
234 estimates of the high frequency spectral slope are very uncertain. More recent work has  
235 found  $\omega^{-2}$  spectral slopes for velocity in extratropical regions but shallower slopes in the  
236 tropics (Scharffenberg and Stammer 2010).

237 Figure 2 shows observed frequency spectra for the same locations discussed above: 35°N,  
238 168°E and 35°N, 222°E. Both locations exhibit a low frequency plateau at periods longer  
239 than 300 days, appear to approach a  $\omega^{-2}$  power law near 100 days, but quickly flatten in  
240 the high frequency tails. The frequency spectrum from AVISO gridded altimetry, linearly  
241 interpolated along the satellite track, is also shown (Fig. 2). The spectrum from AVISO  
242 gridded altimetry is steeper than from un-gridded altimetry at periods shorter than about  
243 110 days.

#### 244 *b. Moored kinetic energy*

245 Frequency spectra of velocity and vertical displacement from moorings are generally  
246 consistent with an  $\omega^{-2}$  slope for periods shorter than 30 days in many regions (Ferrari  
247 and Wunsch 2010). Figure 3 shows observed kinetic energy spectra from moored current  
248 meters at several locations and depths in the North Pacific. Locations are 14°N, 230°E;  
249 28°N, 208°E; 32°N, 232°E; and 39°N, 232°E. Though moorings may be blown-over by strong  
250 currents, leading to measurements at varying depth, no correction for this effect has been  
251 made. All spectra are normalized by the total variance so that the shapes of the spectra can  
252 be easily compared.

253 Overall, a low frequency plateau transitioning to a high frequency  $\omega^{-2}$  power law exists

254 in all the results. However, near 100 day periods, the mooring spectra are flatter than  
 255 similar spectra from altimetry (e.g. Stammer 1997). Strong regional and depth dependent  
 256 differences are seen. For example, the spectral slope tends to become steeper with depth at  
 257 the 28°N mooring. Also, the frequency of the transition from the low frequency plateau to  
 258 a high frequency power law increases with depth at the 39°N mooring.

259 *c. Moored temperature*

260 Figure 4 shows observed temperature spectra from the moored instruments shown in  
 261 Fig. 3. Temperature frequency spectra have a shape generally similar to those for kinetic  
 262 energy. In general, the frequency spectra can again be described as a low frequency plateau  
 263 transitioning to a high frequency  $\omega^{-2}$  power law.

264 The observation that frequency spectra of kinetic energy and temperature have roughly  
 265 the same shape puts an important constraint on the spectrum-model. For some functional  
 266 forms, the characteristic functions for the dynamical model, (9) and (14), would predict  
 267 different spectra for energy and temperature. For example, suppose  $\Phi_\psi \sim (k^2L^2 + l^2L^2 +$   
 268  $\omega^2T^2 + 1)^{-\alpha}$ , where  $L$  and  $T$  are characteristic length and time scales, respectively. After  
 269 multiplying by the appropriate characteristic function and integrating over  $k$  and  $l$ , the  
 270 dynamical model predicts high frequency spectral slopes  $\omega^{4-2\alpha}$  for velocity but  $\omega^{2-2\alpha}$  for  
 271 temperature. In contrast, if  $\Phi_\psi \sim (k^2L^2 + l^2L^2 + 1)^{-\alpha}\omega^{-2}$ , the dynamical model predicts  
 272 frequency spectral slopes  $\omega^{-2}$  for both velocity and temperature. The first functional form  
 273 is inconsistent with observations. This suggests a separable form for the spectrum, at least  
 274 in the frequency and wavenumber range where the spectrum follows an approximate power  
 275 law. However, we have already seen that westward motions dominate (Fig. 1), ruling out  
 276 the possibility of a completely separable spectrum.

277 *d. Shipboard velocity*

278 Wavenumber spectra of kinetic energy are available from both towed and shipboard  
279 Acoustic Doppler Current Profiler (ADCP) instruments, with the latter being more com-  
280 mon. Shipboard measurements in the Gulf Stream show a  $k^{-3}$  spectral slope for kinetic  
281 energy, implying  $k^{-5}$  in SSH for balanced motions (Wang et al. 2010). In the central North  
282 Pacific (25–35°N, 140°W), spectral slopes from shipboard ADCP are close to  $k^{-2}$  for velocity,  
283 implying  $k^{-4}$  for SSH (*J. Callies* 2012, private communication). Both of the in situ spectral  
284 slope estimates are steeper than altimeter-derived estimates in their respective regions (Xu  
285 and Fu 2012), casting doubt on spectral slopes estimated from altimetry at these wavenum-  
286 bers. However, the in situ estimates may include a significant contribution from ageostrophic  
287 motions, complicating the interpretation.

288 Results from a 1000 km section from a meridional transect as part of WOCE section P14N  
289 (180°E, 20°–30°N) at 100 m and span 5 days (Roden 2005) with results in Fig. 5. Tidal or  
290 other ageostrophic motions are not removed from the record. The observed high-wavenumber  
291 spectral slope is close to  $k^{-2}$ , implying  $k^{-4}$  for SSH.

292 Taken together, in situ, altimetric and modeling results are consistent with wavenumber  
293 spectral slopes in the subtropical North Pacific of  $-4 \pm 1$ , with in situ results suggesting  
294 slightly steeper slopes than altimetric results.

295 *e. Vertical structure*

296 Most of what is known about the vertical structure of variability from observations is  
297 based on Wunsch (1997, 1999). Those results support the inference that in the vertical  
298 dimension a modal representation is most useful (a contrast with the internal wave case). The  
299 basic inference was that about 50% of the water-column kinetic energy is in the barotropic  
300 mode, about 40% in the first baroclinic mode, and the remainder in higher baroclinic modes  
301 and noise. The modes were defined as the basic flat-bottom resting ocean Rossby wave

302 modes. However, Wunsch (1997) found evidence of coupling between the modes, such that  
303 the total surface kinetic energy was different from the sum of the energy in each mode. Müller  
304 and Siedler (1992) computed EOFs from several multi-year moorings in the North Atlantic.  
305 The leading EOF generally had a surface-intensified shape, similar to the first baroclinic  
306 mode but no zero crossing. Decomposition into dynamical modes showed coupling between  
307 the barotropic and first baroclinic modes, especially during the most energetic events.

308 Given the short duration of most current meter moorings, almost no observational in-  
309 formation exists about the vertical structure of currents at periods beyond about a year.  
310 Wortham (2013) resorted to GCM results, based on the  $1/6^\circ$  ECCO2 model (Menemenlis  
311 et al. 2008), which suggested that the barotropic and first baroclinic modes are strongly  
312 coupled, especially at interannual periods.

313 The general lack of evidence on which to base conclusions about the vertical structure  
314 of balanced motions has been discussed by Wunsch (2009, 2010) and Ferrari and Wunsch  
315 (2010). In the absence of further observations, we take the evidence from the ECCO2  
316 GCM (Wortham (2013)) as the basis for the spectrum-model vertical structure, presented  
317 in section 5. The vertical structure of balanced motions, especially at periods longer than a  
318 year, deserves further study.

## 319 4. Model $k$ - $l$ - $\omega$ spectrum

320 The spectrum-model presented as a zero-order approximation by Zang and Wunsch  
321 (2001) was universal in shape (only the amplitude changed with location) and separable  
322 in frequency and wavenumber. However, important quantities, such as the first moments of  
323 the spectrum, vary geographically and observations of the nondispersive line are incompati-  
324 ble with a separable form. Many observations are consistent with a single spectral form with  
325 suitable slowly-varying parameters.

326 A quantitatively useful analytical description of the observed spectra is sought, along



327 with some description of its accuracies. For the horizontal wavenumber-frequency spectrum  
 328 discussed in section 3, the structure is captured by,

$$\Phi_\psi(k, l, \omega; \phi, \lambda) = \frac{1}{(k^2 L_x^2 + l^2 L_y^2 + 1)^\alpha (\omega^2 T^2 + 1)} + \exp[-(k^2 L_x^2 + l^2 L_y^2 + T^2(kc_x + lc_y - \omega)^2)] \quad (31)$$

329 where  $\alpha$ ,  $L_x$ ,  $L_y$ ,  $T$ ,  $c_x$ , and  $c_y$  are geographically variable parameters. Equation (31) has  
 330 two parts. A power law appears in the first term, with parameters  $L_x$ ,  $L_y$ , and  $T$  controlling  
 331 the dominant wavelengths and period of the spectrum, while  $\alpha$  sets the high wavenumber  
 332 spectral slope. An exponential term enforces the dominance of westward propagation. The  
 333 exponential term only makes a significant contribution in the range of wavenumber-frequency  
 334 space corresponding to the nondispersive line. This model is entirely empirical, and is judged  
 335 by the authors to provide a reasonable fit to a wide variety of observations described in section  
 336 3. Consistency between the spectrum-model and observations will be discussed below. The  
 337 full spectrum-model is illustrated in Fig. 6 as a set of two-dimensional spectra averaged  
 338 over positive and negative wavenumber half-spaces. Figure 7 displays a three-dimensional  
 339 version.

340 Integrating (31) over  $l$  and  $\omega$  produces the zonal wavenumber spectrum:

$$\begin{aligned} \Phi_\psi(k; \phi, \lambda) &= \int_{-\infty}^{\infty} \int_0^{\infty} \Phi_\psi(k, l, \omega; \phi, \lambda) d\omega dl \quad (32) \\ &= \frac{\pi^{3/2} \Gamma(\alpha - 1/2)}{2TL_y \Gamma(\alpha)} (1 + k^2 L_x^2)^{-\alpha+1/2} + \frac{\pi}{2TL_y} e^{-k^2 L_x^2} \left( 1 + \operatorname{erf} \left[ \frac{kc_x L_y T}{\sqrt{L_y^2 + c_y^2 T^2}} \right] \right) \quad (33) \end{aligned}$$

341 where  $\operatorname{erf}(z)$  is the error function

$$\operatorname{erf}(z) = \frac{2}{\sqrt{\pi}} \int_0^z e^{-t^2} dt, \quad (34)$$

342 with a similar expression for  $\Phi_\psi(l; \phi, \lambda)$ . At high wavenumber, the first term dominates and  
 343 approaches a power law in  $k$  with slope  $-2\alpha + 1$ . Although wavenumber spectral slopes  
 344 from altimetry vary geographically (Xu and Fu 2012), considerable uncertainty exists in the

345 actual values, as discussed in section 3. In light of this uncertainty, a constant  $\alpha = 5/2$   
 346 is used, to be updated when more reliable observations become available. The resulting  
 347 one-dimensional wavenumber spectral slope is  $k^{-4}$  for SSH and  $k^{-2}$  for kinetic energy.

348 Integrating (31) over  $k$  and  $l$  produces the frequency spectrum:

$$\Phi_\psi(\omega; \phi, \lambda) = \int_{-\infty}^{\infty} \int_{-\infty}^{\infty} \Phi_\psi(k, l, \omega; \phi, \lambda) dk dl \quad (35)$$

$$= \frac{\pi}{(\alpha - 1)L_x L_y} (1 + \omega^2 T^2)^{-1} + \frac{\pi}{\sqrt{D}} \exp[-L_x^2 L_y^2 T^2 \omega^2 / D], \quad (36)$$

349 where

$$D = c_x^2 L_y^2 T^2 + L_x^2 L_y^2 + c_y^2 L_x^2 T^2. \quad (37)$$

350 At high frequency, the first term dominates and approaches an  $\omega^{-2}$  power law. This spectral  
 351 slope applies to both SSH and kinetic energy.

352 The most important parameters in the spectrum-model (31) are  $L_x$ ,  $L_y$ , and  $T$ , which  
 353 set the dominant wavelengths and periods. These parameters are chosen such that the first  
 354 moment of the spectrum-model matches inferences from the AVISO product (Fig. 1). From  
 355 (29) with (32) (and the equivalent relations for  $l$ ), the first moment of the wavenumber  
 356 spectrum is

$$\langle k^1 \rangle = \frac{(\alpha - 1) [\sqrt{\pi} \Gamma(\alpha - \frac{3}{2}) + \Gamma(\alpha)]}{L_x \sqrt{\pi} (\alpha + \sqrt{\pi} - 1) \Gamma(\alpha)}, \quad \langle l^1 \rangle = \frac{(\alpha - 1) [\sqrt{\pi} \Gamma(\alpha - \frac{3}{2}) + \Gamma(\alpha)]}{L_y \sqrt{\pi} (\alpha + \sqrt{\pi} - 1) \Gamma(\alpha)}. \quad (38)$$

357 Given  $\langle k^1 \rangle$  and  $\langle l^1 \rangle$  estimated from the AVISO product (Fig. 1),  $L_x$  and  $L_y$  are calculated  
 358 from (38) at each location.

359 The first moment of the frequency spectrum of SSH depends, unfortunately, on the limits  
 360 of integration. Integrating (28) with (35) to an upper frequency limit  $\omega_{\max}$ ,

$$\langle \omega^1 \rangle = \frac{\pi(\alpha - 1)\sqrt{D} (1 - \exp[-\omega_{\max}^2 L_x^2 L_y^2 T^2 / D]) + \pi L_x L_y \ln[1 + \omega_{\max}^2 T^2]}{L_x L_y T (2\pi \arctan(\omega_{\max} T) + \pi^{3/2}(\alpha - 1) \operatorname{erf}[\omega_{\max} L_x L_y T / \sqrt{D}])}. \quad (39)$$

361 Given  $L_x$ ,  $L_y$ , and  $\langle \omega^1 \rangle$  estimated from the AVISO product (Fig. 1), (39) can be solved  
 362 numerically for  $T$  at each location. Here, we use  $\omega_{\max} = 1/14 \text{ days}^{-1}$ , corresponding to the  
 363 Nyquist frequency of the AVISO product.

364 The parameters  $c_x$  and  $c_y$  control the dominant zonal and meridional phase speeds in  
365 the spectrum-model.  $c_x = \omega/k$  is the result of the eigenvalue problem for the vertical  
366 structure, e.g. (3). In practice, the phase speed obtained from the modified eigenvalue  
367 problem discussed in section 5 is used instead. Given the very weak asymmetry between  
368 northward and southward motions, we set  $c_y = 0$  everywhere.

369 The spectrum-model (31) is intended to approximate the observed spectrum for peri-  
370 ods between the inertial period and about 10 years, and wavelengths between 100 km and  
371 10,000 km. These limits are primarily set by the duration and spatial resolution of the al-  
372 timetric product that was used to inform the spectrum-model (Chelton et al. 2011). The  
373 important question of the behavior of the frequency spectrum as  $\omega$  approaches zero is be-  
374 yond the scope of this work, but has been discussed elsewhere (Wunsch 2010, and references  
375 therein). As  $\omega \rightarrow 0$  the spectrum-model here becomes white in frequency with consequences  
376 for trend determination. In the remainder of this section, the predictions of (31) are com-  
377 pared with various observed spectra.

#### 378 *a. Global patterns*

379 The spectrum-model (31) is spatially variable, resulting in realistic patterns of dominant  
380 phase speed, period, and wavelength (Fig. 8), with values comparable to Fig. 1. The main  
381 difference is between phase speeds from AVISO and the spectrum-model; the eigenvalue  
382 problem used to set  $c_x$  in the spectrum-model does not permit eastward phase speeds.

#### 383 *b. Along-track altimetry*

384 Figure 2 compares wavenumber spectra of SSH from the spectrum-model and altimetry.  
385 The spectrum-model is normalized such that it has the same total variance as the observed  
386 one. In both regions, the model captures the general shape of the observed spectrum at  
387 wavelengths larger than 200 km. In particular, the transition from plateau to power law

388 occurs at the same wavelength in the spectrum-model as in the altimetric spectrum. The  
389 model has a constant high-wavenumber spectral slope of  $k^{-4}$  for SSH and does not agree  
390 with the altimetric spectra for scales smaller than about 200 km, where the observations are  
391 contaminated by measurement noise (Xu and Fu 2012).

392 Figure 2 also shows modeled frequency spectra for the same locations. Again, the  
393 spectrum-model transitions from plateau to power law at the same frequency as the alti-  
394 metric spectrum, and the  $\omega^{-2}$  power law is a reasonable fit for periods longer than about  
395 60 days. The frequency of the transition is set by the parameter  $T$ . At shorter periods the  
396 spectrum from along-track altimetry flattens, but the spectrum-model follows the spectrum  
397 from AVISO.

#### 398 *c. Moored kinetic energy*

399 Figure 3 shows normalized modeled kinetic energy spectra at several locations and depths  
400 in the North Pacific. Overall, the spectrum-model follows the observed values, and captures  
401 the transition from plateau to  $\omega^{-2}$  power law and, over most of the frequency range, is  
402 within the estimated uncertainty of the observed spectra. Although Fig. 3 suggests that the  
403 spectral shape changes with depth, these changes are not statistically significant given the  
404 available data, and are not reflected in (31).

405 As  $\omega$  approaches  $f/2\pi$  from below, the observed spectrum (Fig. 9) transitions smoothly  
406 into the internal wave regime at frequencies not modeled here. The transition regime between  
407 the present model and the Garrett-Munk spectrum, plus tidal and inertial peaks, remains  
408 to be properly represented, an effort not undertaken here.

#### 409 *d. Moored temperature*

410 Figure 4 shows normalized temperature spectra from the moored instruments shown in  
411 Fig. 3. Again, for most instruments, the spectrum-model follows the observed spectra within

412 the estimated uncertainty of the latter.

413 *e. Shipboard velocity*

414 The model wavenumber spectrum of kinetic energy is shown in Fig. 5. At this location,  
415 the spectrum-model amplitude was lower than the observed by a factor of 2 and is normalized  
416 to have the same total variance as the observations so the spectral shape can be compared.  
417 The model  $k^{-2}$  spectral slope is close to that observed, and the spectrum-model is within  
418 the estimated uncertainty of the observed spectrum at all wavelengths.

## 419 **5. Model vertical structure**

420 The vertical structure of the spectrum-model proposed by Zang and Wunsch (2001) was  
421 largely based on the observations of Wunsch (1997). They used the representation of (3)  
422 under BTT boundary conditions with mode partition  $E(0) = 1$ ,  $E(1) = 1$ ,  $E(2) = 1/2$ , and  
423  $E(n) = 0$  for  $n \geq 3$  in (20). While this recipe works in some locations (Zang and Wunsch  
424 2001), it has a strong tendency to overestimate kinetic energy in the abyss and underestimate  
425 kinetic energy near the surface. That is, kinetic energy is more surface intensified than their  
426 vertical structure predicted. Wortham (2013) suggests that such a systematic misfit to the  
427 observed kinetic energy profile is indicative of coupling between the barotropic and baroclinic  
428 modes.

429 Several dynamical processes have been proposed to explain the surface intensification of  
430 kinetic energy. These include the impact of mean flow (Keller and Veronis 1969; Killworth  
431 et al. 1997; Dewar 1998; de Szoeke and Chelton 1999; Killworth and Blundell 2004, 2005),  
432 large scale sloping topography (Killworth and Blundell 1999), small scale rough topography  
433 (Rhines and Bretherton 1973; Samelson 1992; Bobrovich and Reznik 1999; Tailleux and  
434 McWilliams 2001), surface forcing by Ekman pumping (Frankignoul and Müller 1979b,a;  
435 Müller and Frankignoul 1981; Killworth and Blundell 2007), SQG dynamics (Lapeyre and

436 Klein 2006; LaCasce 2012), and nonlinearity (McWilliams and Flierl 1979; Vanneste 2003;  
 437 Chelton et al. 2007, 2011). See Wortham (2013) and references therein for a more complete  
 438 discussion. We focus on the roles of mean flow and rough topography because they predict  
 439 the observed vertical structure, while recognizing that other dynamics may be important  
 440 too.

441 Samelson (1992) found that rough topography produced surface intensified Rossby waves  
 442 in a 2-layer model, and Bobrovich and Reznik (1999) provided an analytical description of the  
 443 effect in a constant stratification. The latter showed that rough topography reduces the wave  
 444 amplitude near the bottom, though this analytical theory is difficult to apply for realistic  
 445 stratification. Tailleux and McWilliams (2001) have presented a simple approximation of the  
 446 impact of topography through their “bottom pressure decoupling” (BPD) theory. Essentially,  
 447 the BPD formulation replaces the standard bottom boundary condition,  $dF/dz = 0$ , with  
 448  $F(z) = 0$  at  $z = -H$ . Aoki et al. (2009) showed that this BPD theory and mean flow both  
 449 improved the representation of vertical structure in a GCM.

450 Consider the quasi-geostrophic vorticity equation, linearized about the local mean state  
 451  $\mathbf{U} = U(z)\mathbf{i} + V(z)\mathbf{j}$  (Aoki et al. 2009),

$$\begin{aligned} \left[ \frac{\partial}{\partial t} + U \frac{\partial}{\partial x} + V \frac{\partial}{\partial y} \right] \left[ \nabla^2 \psi + \frac{\partial}{\partial z} \left( \frac{f_0^2}{N^2} \frac{\partial \psi}{\partial z} \right) \right] - \frac{\partial}{\partial z} \left( \frac{f_0^2}{N^2} \frac{\partial V}{\partial z} \right) \frac{\partial \psi}{\partial y} \\ + \left[ \beta - \frac{\partial}{\partial z} \left( \frac{f_0^2}{N^2} \frac{\partial U}{\partial z} \right) \right] \frac{\partial \psi}{\partial x} = 0, \quad -H < z < 0. \end{aligned} \quad (40)$$

452 Imposing wave solutions in the form  $\psi(x, y, z, t) = F(z)e^{-i2\pi(kx+ly-\omega t)}$  in (40), the vertical  
 453 structure satisfies

$$\begin{aligned} (\mathbf{K} \cdot \mathbf{U} - \omega) \left[ \frac{\partial}{\partial z} \left( \frac{f_0^2}{N^2} \frac{\partial}{\partial z} \right) - K^2 \right] F(z) = \\ \left[ l \frac{\partial}{\partial z} \left( \frac{f_0^2}{N^2} \frac{\partial V}{\partial z} \right) - k \left( \beta - \frac{\partial}{\partial z} \left( \frac{f_0^2}{N^2} \frac{\partial U}{\partial z} \right) \right) \right] F(z), \end{aligned} \quad (41)$$

454 where  $\mathbf{K} = (k, l)$  and  $K = \sqrt{k^2 + l^2}$ . Given the mean flow  $\mathbf{U}$ , stratification  $N^2$ , and  
 455 suitable boundary conditions, (41) forms an eigenvalue problem which can be solved for  
 456 the eigenmodes  $F_n(z)$  and eigenvalues  $\omega_n$ ,  $n = 0, 1, 2, \dots$

457 Following the formulation of Aoki et al. (2009), including the effects of mean flow and  
 458 BPD, the vertical modes are the eigenmodes of (41) subject to the boundary conditions

$$\frac{dF}{dz} = 0 \quad \text{at} \quad z = 0, \quad (42)$$

$$F = 0 \quad \text{at} \quad z = -H. \quad (43)$$

459 We use  $l = 0$  and  $k = 1/(100L_d)$ , effectively in the long-wave limit, where  $L_d$  is BTT first  
 460 baroclinic mode deformation radius. Mean flow  $\mathbf{U}$ , salinity  $S$ , and potential temperature  $\theta$   
 461 are taken from the OCCA atlas (Forget 2010), and stratification is computed using a neutral  
 462 density calculation (Chelton et al. 1998).

463 Comparison with vertical profiles of EKE and temperature variation at the four mooring  
 464 sites shown in Figs. 3 and 4 produced a reasonable fit with the mode coefficients  $E(0) = 1/2$ ,  
 465  $E(1) = 1$ ,  $E(2) = 1/4$ ,  $E(3) = 1/10$ ,  $E(n) = 0$  for  $n \geq 4$ . These coefficients are then used  
 466 globally. The coefficients  $E(n)$  used here are preliminary, and the representation of the  
 467 vertical structure in the spectrum-model deserves further study. The resulting spectrum-  
 468 model vertical structure is discussed below.

469 A possible significant shortcoming of the representation in (20) is the assumption that  
 470 the vertical structure is independent of period/wavelength. In almost all extensions (e.g.  
 471 Tailleux and McWilliams (2001); Killworth and Blundell (2004); Lapeyre and Klein (2006)),  
 472 vertical mode structure depends on wavelength. With existing observational technologies,  
 473 the period/wavelength dependence of the vertical structure will be very difficult to determine.

#### 474 *EKE(z) and $\sigma_\theta(z)$ profiles*

475 The Appendix describes by example how to compute various quantities from the spectrum-  
 476 model. Here some summary comparisons with other observations are made. Figure 10 com-  
 477 pares the vertical profile of kinetic energy for the spectrum-model with sub-inertial kinetic  
 478 energy from the set of current meters discussed in section 3b. Sub-inertial kinetic energy is  
 479 estimated by integrating its spectrum over frequencies below  $1/5$  cpd for each instrument,

480 and a similar estimate is made from the model. For most instruments, the model kinetic en-  
481 ergy agrees with the observed to within a factor of 2, indicated by gray shading in the figure,  
482 and often better. The main exception is near 1000 m at 28°N, where the model overestimates  
483 the observed kinetic energy by a factor of 3.

484 Figure 11 compares the vertical profile of temperature standard deviation  $\sigma_\theta$  for the  
485 spectrum-model with observations from moored temperature sensors. The predicted tem-  
486 perature standard deviation is within a factor of 2 of the observations in almost all cases,  
487 as indicated by gray shading in the figure. An example of the calculation of temperature  
488 standard deviation is reproduced in the Appendix.

489 For a further evaluation of spectrum-model, we expand the analysis to the large number  
490 of moored current meter and temperature sensors collected in the Global Multi-Archive  
491 Current Meter Database (CMD) (Scott et al. 2010). We found 4112 current meter records  
492 with a duration of at least 180 days moored in water deeper than 1000 m and with nominal  
493 instrument depth at least 500 m above the sea floor. From this set, we excluded records with  
494 quality control flags set in the original archive, records with less than 50% data coverage,  
495 and instruments within 5° of the equator or 2.5° of land. These criteria resulted in 2179  
496 current meter records and 1948 temperature records included in the analysis. The locations  
497 of these instruments are mapped in Fig. 12.

498 The sampling frequencies for the records analyzed vary from 5 min to 1 day. To produce  
499 homogeneous records for comparison with the spectrum-model, all records are reduced to  
500 5 day moving averages. When there are missing data in a 5 day window, the average is  
501 computed as long as there are at least 2.5 days of good data within the window; otherwise,  
502 the time period is flagged as missing and no temporal interpolation is made. For each 5 day  
503 averaged time series, we compute the EKE and temperature standard deviation  $\sigma_\theta$ . For each  
504 record, EKE and  $\sigma_\theta$  are computed from the spectrum-model at the instrument location and  
505 depth.

506 Scatterplots compare the EKE and  $\sigma_\theta$  from the spectrum-model with the CMD records



507 (Fig. 13). If there were perfect agreement between the spectrum-model and the CMD records,  
508 all points would fall along the 45° line. For EKE, there is strong correlation between the  
509 spectrum-model and observed values (Pearson correlation coefficient  $r = 0.85$ ). Conspicuous  
510 in the EKE scatterplot is a cluster of points well below the 45° line, with the spectrum-model  
511 underestimating the observed EKE. At these points the spectrum-model vertical structure  
512 for EKE is very surface intensified. This surface intensification is caused by the local mean  
513 flow  $\mathbf{U}$  in (41). Strong, presumably unrealistic surface intensification in the spectrum-model  
514 occurred in about 50 cases. For  $\sigma_\theta$ , the correlation is weaker ( $r = 0.77$ ) and the spectrum-  
515 model is biased high. Both correlations are highly statistically significant ( $P < 10^{-4}$ ).

516 Biases in the spectrum-model are revealed by examining the following statistic, similar  
517 to that used by Scott et al. (2010):

$$D_{\text{EKE}} = \frac{\text{EKE}_{\text{CMD}} - \text{EKE}_{\text{MOD}}}{\text{EKE}_{\text{CMD}} + \text{EKE}_{\text{MOD}}}, \quad (44)$$

$$D_{\sigma_\theta} = \frac{\sigma_{\theta,\text{CMD}} - \sigma_{\theta,\text{MOD}}}{\sigma_{\theta,\text{CMD}} + \sigma_{\theta,\text{MOD}}}, \quad (45)$$

518 where subscripts CMD and MOD indicate values from observations and the spectrum-model,  
519 respectively. This statistic maps the discrepancy onto the interval  $[-1, 1]$ . For perfect agree-  
520 ment between the spectrum-model and observations,  $D_{\text{EKE}}$  and  $D_{\sigma_\theta}$  would be distributed  
521 like the Dirac- $\delta$  function.

522 Figure 14 shows histograms of  $D_{\text{EKE}}$  and  $D_{\sigma_\theta}$ , grouped by instrument depth. Depth bins  
523 are 0–700 m, 700–3000 m, and below 3000 m. The depth bins are selected to give roughly  
524 equal numbers of instruments in each bin. Overall, EKE from the spectrum-model is slightly  
525 stronger than from the CMD, with the strongest bias in the 700–3000 m bin. The distri-  
526 bution of  $D_{\sigma_\theta}$  reveals the depth-dependence of the spectrum-model bias. Above 700 m, the  
527 spectrum-model  $\sigma_\theta$  tends to be smaller than observed, while between 700 and 3000 m, the  
528 spectrum-model  $\sigma_\theta$  tends to be larger. Below 3000 m, the spectrum model has a strong  
529 bias toward high  $\sigma_\theta$ . Median values for  $D_{\text{EKE}}$  and  $D_{\sigma_\theta}$  in each depth bin represent the  
530 spectrum-model bias (Table 1).

## 531 6. Applications

532 Many potential applications, both theoretical and practical, exist for the spectrum-model.  
533 At the core of the theoretical applications lies the need to explain why it takes on the char-  
534 acteristics it does, including power laws, dispersion curves, and modal coupling. Although  
535 some of these have been touched upon in the discussion of the construction of the model,  
536 these and similar questions are not pursued further here. The model can also be used to  
537 predict spectral energy and enstrophy fluxes, as in Scott and Wang (2005) and Arbic et al.  
538 (2012). Finally, the spectrum-model can be used to estimate isopycnal eddy diffusivities.  
539 Following Taylor (1921), diffusivity due to mesoscale eddies can be expressed in terms of  
540 the Lagrangian velocity autocorrelation function which, in turn, can be estimated from the  
541 spectrum-model (Davis 1982; Zang 2000).

542 The spectral representation is also useful in discussions of space-time sampling require-  
543 ments for a variety of physical parameters, including the variability of volume flux across  
544 a latitude line or heat content, determination of the accuracy of estimated values, and the  
545 significance of any observed purported trends. As one illustration of this type of application,  
546 Wunsch (2008) used estimates of eddy variability to show that time series of meridional trans-  
547 port calculated from a pair of moorings spanning the North Atlantic will exhibit stochastic  
548 fluctuations with multi-year time scales. Such stochastic fluctuations complicate the task of  
549 identifying secular trends in the ocean circulation related to climate change. Equation (31)  
550 can also be used to predict unobserved spectra, such as for the wavenumbers of vertical  
551 displacement.

552 Many practical applications of the spectrum-model rely on estimates of space and time  
553 correlation functions, given by (24). The one-dimensional correlation functions of tempera-  
554 ture as a function of zonal, meridional, and temporal separation are shown in Fig. 15. At  
555  $30^{\circ}\text{N}$ ,  $190^{\circ}\text{E}$ , the correlations show approximately exponential decay, with e-folding wave-  
556 length of 125 km for zonal separation, 110 km for meridional separation, and 40 days for  
557 temporal separation.

558 The correlation function is useful, for example, in objective mapping of satellite and in  
559 situ data. In this context, the spectrum-model provides an estimate of the signal covariance.  
560 In objective mapping, the goal is to estimate the value of a field,  $\chi$ , at a general point  $\tilde{r}$  given  
561 a set of measurements  $y$  at positions  $r_i$ . While simple linear interpolation is often used, more  
562 general methods (e.g. Bretherton et al. 1976; Wunsch 2006, §3.2) make use of covariances  
563 within the signal and noise, which can be estimated from the spectrum-model.

564 Using (27), we plot the meridional velocity coherence at 30°N, 190°E for meridional  
565 separations between 0 and 200 km (Fig. 16). Since the spectral shape is independent of depth,  
566 the predicted coherence is the same at all depths. As expected from the autocorrelation  
567 function, there is little coherence for separation beyond about 100 km. An example coherence  
568 calculation is reproduced in the Appendix.

569 Finally, the model is applicable to observing system design and trend detection. In this  
570 context, the spectrum provides the noise covariance. One can estimate, for example, the  
571 number of deep Argo floats needed to detect temperature trends in the abyssal ocean over a  
572 given time period. This and other applications are left for future study.

## 573 **7. Discussion**

574 A strawman empirical model of the four-dimensional spectral density of low frequency  
575 (longer than about 20 days but shorter than a decade) ocean variability is proposed. The  
576 model is based on a variety of observations, including satellite altimetry, moored temperature  
577 and current meters, and shipboard velocity measurements. A model of the spectrum of the  
578 geostrophic streamfunction is presented, and compared with observations assuming simple  
579 geostrophic dynamics. However, many regions of the ocean have peculiar dynamics where  
580 the model is inaccurate. In particular, no attempt is made to match observations in the  
581 near-surface mixed layer, the core of western boundary currents, the Antarctic Circumpolar  
582 Current, within about 5° of the equator, or poleward of 50°.

583 For the horizontal wavenumber-frequency portion of the spectrum, an implicit two-scale  
584 approximation is made; a locally uniform spectrum is modulated by slowly varying geo-  
585 graphical parameters  $L_x$ ,  $L_y$ ,  $T$ , and  $c_x$ . These parameters determine the dominant space  
586 and time scales of the spectrum, as well as a dominant propagation direction. In this way,  
587 a single analytical expression (31) represents the shape of the spectrum over much of the  
588 ocean. A typical spectrum is shown in Fig. 6.

589 The amplitude of the spectrum-model is set to match altimetric observations of the sur-  
590 face eddy kinetic energy. The depth dependence is expressed in terms of Rossby wave vertical  
591 modes modified to account for the effects of mean flow and rough topography (Tailleux and  
592 McWilliams 2001; Aoki et al. 2009). Including these two effects greatly improves the agree-  
593 ment with observations over the conventional flat-bottom, resting ocean theory which does  
594 not capture the observed surface intensification of kinetic energy. The possibility that other  
595 dynamical processes (e.g., the generation of strongly surface-intensified eddies by baroclinic  
596 instability) contribute to the observed vertical structure is not excluded.

597 Explanation of the energy levels and spectral shape is not the goal here. We can, how-  
598 ever, speculate to a degree on the basis of known theories. Müller and Frankignoul (1981)  
599 present a detailed analysis of the frequency spectrum of the quasi-geostrophic oceanic re-  
600 sponse to atmospheric forcing. The resulting spectrum is the integral response of the ocean  
601 to continuous random forcing by the atmosphere. Their predicted spectrum is white at low  
602 frequencies, changing smoothly to a  $\omega^{-2}$  power law at  $\omega \sim \omega_n^{\max}$  (their Fig. 7). The maxi-  
603 mum frequency for the first baroclinic mode,  $\omega_1^{\max} = \beta L_d/2$ , depends on latitude primarily  
604 through the deformation radius  $L_d$ . Thus, they predict that the break point between the  
605 white low frequency spectrum and  $\omega^{-2}$  power law will decrease with latitude as the defor-  
606 mation radius decreases. The general shape predicted by Müller and Frankignoul (1981) is  
607 similar to the model frequency spectrum presented here.

608 For the wavenumber spectrum of total energy in the  $n^{\text{th}}$  mode, Müller and Frankignoul

609 (1981) predict

$$E_{\text{tot}}^n \sim \frac{1}{k^3 + kL_d^{-2}}. \quad (46)$$

610 For the baroclinic modes, the spectrum transitions from a  $k^{-1}$  power law at low wavenumber  
611 to a steeper  $k^{-3}$  at high wavenumber with the break point near the deformation radius. For  
612 the barotropic mode, the predicted spectrum is a  $k^{-3}$  power law at high wavenumber. This  
613 is steeper than the  $k^{-2}$  in the spectrum-model presented here.

614 The character of low frequency variability can also be attributed to quasi-geostrophic  
615 (QG) turbulence theory. QG turbulence theory predicts a forward enstrophy cascade for  
616 wavenumbers higher than the energy injection scale  $k_I$  (Charney 1971), and an inverse energy  
617 cascade for lower wavenumbers. The kinetic energy spectra in the forward and inverse ranges  
618 are

$$E(k) \sim k^{-3} \quad \text{for} \quad |k| > k_I, \quad (47)$$

$$E(k) \sim k^{-5/3} \quad \text{for} \quad |k| < k_I. \quad (48)$$

619 For balanced motions, this requirement implies a  $k^{-5}$  power law for SSH for  $|k| > k_I$ ,  
620 and  $k^{-11/3}$  for  $|k| < k_I$ . The energy injection wavenumber appears to be close to the  
621 deformation scale (Scott and Wang 2005). A considerable literature compares observed  
622 wavenumber spectra with the predictions of turbulence theories (e.g. Stammer 1997; Le Traon  
623 et al. 2008; Lapeyre 2009; Wang et al. 2010; Xu and Fu 2012). Further, eddy generation  
624 through baroclinic instability has shown skill in predicting observed wavelengths of variability  
625 (Tulloch et al. 2011) and seasonal modulation of EKE (Qiu et al. 2008).

626 Some inconvenient evidence has been ignored here. Most important, the model assumes  
627 that variability is due to the superposition of a random wave field, excluding evidence for  
628 “coherent motions” (Chelton et al. 2011; Early et al. 2011). Structures such as isolated  
629 vortices, where present, would significantly increase the expected variance relative to a ran-  
630 dom wave field by phase-locking different horizontal wavelengths and frequencies. These  
631 effects could be addressed by estimating higher-order spectra, such as the bispectrum and

632 trispectrum, which describe nonlinear interactions between spectral components.

633 Despite the shortcomings of the present model, it has reached a stage where it can  
634 be usefully applied in a variety of areas. Obvious applications include the estimation of  
635 uncertainties in observed trends, observing system design, objective mapping of data, and  
636 evaluating the scales of variability produced in ocean GCMs.

637 *Acknowledgments.*

638 We thank R. Ferrari, G. Flierl, and S. Jayne for helpful comments. Moored current  
639 meter and temperature sensor data were provided by R. Scott and D. Furnival through the  
640 Global Multi-Archive Current Meter Database. The altimeter products were produced by  
641 SSALTO/DUACS and distributed by AVISO, with support from CNES. This research was  
642 supported by NASA under grants NNG06GC28G and NNX08AR33G.

643

644

645

## Working with the spectrum-model

646

647

648

649

650

Although the shape of the spectrum-model is easily computed from (31) integrated over frequency or wavenumber, calculating the absolute amplitude is more complicated. Here, we show by example how to use the spectrum-model to predict quantitative values (e.g., variance) for different variables. The variance predicted by the spectrum-model for a generic variable  $\chi$  at depth  $z$  is

$$\sigma_{\chi}^2(z) = \int_0^{\infty} \int_{-\infty}^{\infty} \int_{-\infty}^{\infty} \Phi_{\chi}(k, l, \omega, z; \phi, \lambda) dk dl d\omega. \quad (\text{A1})$$

651

By (17) and (20),

$$\sigma_{\chi}^2(z) = I(\phi, \lambda) \sum_n E(n) \int_0^{\infty} \int_{-\infty}^{\infty} \int_{-\infty}^{\infty} |\tilde{\chi}|^2 \Phi_{\psi}(k, l, \omega; \phi, \lambda) dk dl d\omega, \quad (\text{A2})$$

652

653

654

655

where  $\Phi_{\psi}(k, l, \omega; \phi, \lambda)$  is the three dimensional spectrum-model (31). The characteristic functions (8)-(14) are separable:  $\tilde{\chi} = \hat{\chi}(k, l, \omega)\bar{\chi}(z)$ , and we define  $\hat{p} = \hat{\rho} = \hat{\zeta} = \hat{\theta} = 1$ ,  $\hat{u} = l$ ,  $\hat{v} = k$  and  $\hat{w} = \omega$ . All other factors are grouped with the vertical part  $\bar{\chi}(z)$ , e.g.,  $\bar{\theta}(z) = i2\pi F_n(z)$ . With this separation, the variance is

$$\sigma_{\chi}^2(z) = I(\phi, \lambda) \int_0^{\infty} \int_{-\infty}^{\infty} \int_{-\infty}^{\infty} |\hat{\chi}|^2 \Phi_{\psi}(k, l, \omega; \phi, \lambda) dk dl d\omega \times \sum_n E(n) |\bar{\chi}|^2, \quad (\text{A3})$$

656

657

where the first two factors are a horizontally varying intensity, and the last represents the vertical structure. (Horizontal variation in the vertical mode shape is implicit.)

658

659

660

661

662

Four possible maps of the horizontally varying part of (A3) exist, corresponding to the four functional forms of  $\hat{\chi}$  (Fig. 17). These maps primarily reflect the variation in EKE through  $I(\phi, \lambda)$ , but also depend on the spatially variable shape of the spectrum through the parameters  $L_x$ ,  $L_y$ , and  $T$ . The vertical structure part of (A3) depends on location and the specific variable.

663 As an example of the use of the spectrum-model, maps in Fig. 17 can be combined with  
 664 the appropriate vertical structure to estimate variability at a given depth. The vertical  
 665 structure for temperature,  $\sum_n E(n) |f_0 G_n(z) \partial \theta_0 / \partial z|^2$  is shown in Fig. 18 near 39°N, 230°E.  
 666 At this location and 500 m depth,  $I \iiint \Phi_\psi dk dl d\omega = 1.4 \times 10^6 \text{ m}^4 \text{ s}^{-2}$  and  $\sum E(n) |\bar{\theta}|^2 =$   
 667  $1 \times 10^{-8} \text{ }^\circ \text{C}^2 \text{ s}^2 \text{ m}^{-4}$  so that  $\sigma_\theta(500 \text{ m}) = 0.12 \text{ }^\circ \text{C}$  as in Fig. 11.

668 Coherence from the spectrum-model is given by (27) and depends on  $F_n(z)$  through the  
 669 characteristic function and  $I(\phi, \lambda)$  through (20), quantities which are difficult to compute  
 670 in general. Using the separation  $\tilde{\chi} = \hat{\chi}(k, l, \omega) \bar{\chi}(z, n)$  introduced above with (17) and (20),  
 671 (27) is

$$Coh(\omega; r_x, r_y, z, z') = \frac{C(z) \int_{-\infty}^{\infty} \int_{-\infty}^{\infty} \hat{\chi} \hat{\Upsilon}^* \Phi_\psi(k, l, \omega; \phi, \lambda) e^{i2\pi(kr_x + lr_y)} dk dl}{\sqrt{\left[ \int_{-\infty}^{\infty} \int_{-\infty}^{\infty} |\hat{\chi}|^2 \Phi_\psi(k, l, \omega; \phi, \lambda) dk dl \right] \left[ \int_{-\infty}^{\infty} \int_{-\infty}^{\infty} |\hat{\Upsilon}|^2 \Phi_\psi(k, l, \omega; \phi, \lambda) dk dl \right]}}, \quad (\text{A4})$$

672 where

$$C(z) = \frac{\sum_{n=0}^{\infty} \bar{\chi} \bar{\Upsilon}^* E(n)}{\sqrt{\left[ \sum_{n=0}^{\infty} |\bar{\chi}|^2 E(n) \right] \left[ \sum_{n=0}^{\infty} |\bar{\Upsilon}|^2 E(n) \right]}}, \quad (\text{A5})$$

673 contains the depth dependence. In general,  $C(z)$  depends on the vertical structure functions  
 674  $F_n(z)$  and  $G_n(z)$ , and is difficult to compute. However, in the common case of auto-coherence,  
 675  $\chi = \Upsilon$ ,  $C(z) = 1$ . In this case, the coherence can be computed from the spectrum-model  
 676 (31) and  $\hat{\chi}$  part of the characteristic function, integrated over all wavenumbers.



## REFERENCES

- 679 Aoki, K., A. Kubokawa, H. Sasaki, and Y. Sasai, 2009: Midlatitude baroclinic Rossby waves  
680 in a high-resolution OGCM simulation. *Journal of Physical Oceanography*, **39** (9), 2264–  
681 2279.
- 682 Arbic, B. K., R. B. Scott, G. R. Flierl, A. J. Morten, J. G. Richman, and J. F. Shriver, 2012:  
683 Nonlinear cascades of surface oceanic geostrophic kinetic energy in the frequency domain.  
684 *Journal of Physical Oceanography*, **42** (9), 1577–1600, doi:10.1175/JPO-D-11-0151.1.
- 685 Bobrovich, A. V. and G. M. Reznik, 1999: Planetary waves in a stratified ocean of variable  
686 depth. Part 2. Continuously stratified ocean. *Journal of Fluid Mechanics*, **388**, 147–169.
- 687 Bretherton, F., R. Davis, and C. Fandry, 1976: A technique for objective analysis and design  
688 of oceanographic experiments applied to MODE-73. *Deep Sea Research and Oceanographic*  
689 *Abstracts*, **23** (7), 559–582, doi:10.1016/0011-7471(76)90001-2.
- 690 Charney, J. G., 1971: Geostrophic turbulence. *Journal of the Atmospheric Sciences*, **28**,  
691 1087–1097.
- 692 Chelton, D. B., R. A. de Szoeke, M. G. Schlax, K. El Naggar, and N. Siwertz, 1998: Geo-  
693 graphical variability of the first baroclinic Rossby radius of deformation. *Journal of Phys-*  
694 *ical Oceanography*, **28** (3), 433–460.
- 695 Chelton, D. B. and M. G. Schlax, 1996: Global observations of oceanic Rossby waves.  
696 *Science*, **272** (5259), 234–238.
- 697 Chelton, D. B., M. G. Schlax, and R. M. Samelson, 2011: Global observations of nonlinear  
698 mesoscale eddies. *Progress in Oceanography*, **91** (2), 167–216, doi:10.1016/j.pocean.2011.  
699 01.002.

- 700 Chelton, D. B., M. G. Schlax, R. M. Samelson, and R. A. de Szoeke, 2007: Global observa-  
701 tions of large oceanic eddies. *Geophysical Research Letters*, **34**, L15 606.
- 702 Chiswell, S. M. and G. J. Rickard, 2008: Eulerian and Lagrangian statistics in the Bluelink  
703 numerical model and AVISO altimetry: Validation of model eddy kinetics. *Journal of*  
704 *Geophysical Research*, **113 (C10)**, doi:10.1029/2007JC004673.
- 705 Davis, R. E., 1982: On relating Eulerian and Lagrangian velocity statistics: single  
706 particles in homogeneous flows. *Journal of Fluid Mechanics*, **114**, 1–26, doi:10.1017/  
707 S0022112082000019.
- 708 de Szoeke, R. A. and D. B. Chelton, 1999: The modification of long planetary waves by  
709 homogeneous potential vorticity layers. *Journal of Physical Oceanography*, **29 (3)**, 500–  
710 511.
- 711 Dewar, W. K., 1998: On “too fast” baroclinic planetary waves in the general circulation.  
712 *Journal of Physical Oceanography*, **28 (9)**, 1739–1758.
- 713 Ducet, N., P.-Y. Le Traon, and G. Reverdin, 2000: Global high-resolution mapping of ocean  
714 circulation from TOPEX/POSEIDON and ERS-1 and -2. *Journal of Geophysical Research*,  
715 **105 (C8)**, 19 477–19 498.
- 716 Early, J. J., R. M. Samelson, and D. B. Chelton, 2011: The evolution and propagation of  
717 quasigeostrophic ocean eddies. *Journal of Physical Oceanography*, **41 (8)**, 1535–1555.
- 718 Ferrari, R. and C. Wunsch, 2010: The distribution of eddy kinetic and potential energies in  
719 the global ocean. *Tellus*, **62 (2)**, 92–108.
- 720 Forget, G., 2010: Mapping ocean observations in a dynamical framework: a 2004–2006 ocean  
721 atlas. *Journal of Physical Oceanography*, **40 (6)**, 1201–1221.
- 722 Frankignoul, C. and P. Müller, 1979a: On the generation of geostrophic eddies by surface  
723 buoyancy flux anomalies. *Journal of Physical Oceanography*, **9 (6)**, 1207–1213.

724 Frankignoul, C. and P. Müller, 1979b: Quasi-geostrophic response of an infinite -plane ocean  
725 to stochastic forcing by the atmosphere. *Journal of Physical Oceanography*, **9 (1)**, 104–127.

726 Ganachaud, A., 2003: Large-scale mass transports, water mass formation, and diffusivities  
727 estimated from World Ocean Circulation Experiment (WOCE) hydrographic data. *Journal*  
728 *of Geophysical Research*, **108 (C7)**, doi:10.1029/2002JC001565.

729 Garrett, C. and W. Munk, 1972: Space-time scales of internal waves. *Geophysical Fluid*  
730 *Dynamics*, **2**, 225–264.

731 Garrett, C. and W. Munk, 1975: Space-time scales of internal waves: a progress report.  
732 *Journal of Geophysical Research*, **80 (3)**, 291–297.

733 Gill, A. E., 1982: *Atmosphere-Ocean Dynamics*, International Geophysics Series, Vol. 30.  
734 Academic Press, San Diego.

735 Hughes, C. W. and S. D. P. Williams, 2010: The color of sea level: Importance of spatial  
736 variations in spectral shape for assessing the significance of trends. *Journal of Geophysical*  
737 *Research*, **115**, C10 048.

738 Jacobs, G. A., C. N. Barron, and R. C. Rhodes, 2001: Mesoscale characteristics. *Journal of*  
739 *Geophysical Research*, **106 (C9)**, 19 581–19 595, doi:10.1029/2000JC000669.

740 Keller, J. B. and G. Veronis, 1969: Rossby waves in the presence of random currents. *Journal*  
741 *of Geophysical Research*, **74 (8)**, 1941–1951, doi:10.1029/JB074i008p01941.

742 Killworth, P. D. and J. R. Blundell, 1999: The effect of bottom topography on the speed  
743 of long extratropical planetary waves. *Journal of Physical Oceanography*, **29 (10)**, 2689–  
744 2710.

745 Killworth, P. D. and J. R. Blundell, 2004: The dispersion relation for planetary waves in  
746 the presence of mean flow and topography. Part I: Analytical theory and one-dimensional  
747 examples. *Journal of Physical Oceanography*, **34 (12)**, 2692–2711.

- 748 Killworth, P. D. and J. R. Blundell, 2005: The dispersion relation for planetary waves in  
749 the presence of mean flow and topography. Part II: Two-dimensional examples and global  
750 results. *Journal of Physical Oceanography*, **35** (11), 2110–2133.
- 751 Killworth, P. D. and J. R. Blundell, 2007: Planetary wave response to surface forcing and  
752 instability in the presence of mean flow and topography. *Journal of Physical Oceanography*,  
753 **37** (5), 1297–1320.
- 754 Killworth, P. D., D. B. Chelton, and R. A. de Szoeke, 1997: The speed of observed and  
755 theoretical long extratropical planetary waves. *Journal of Physical Oceanography*, **27** (9),  
756 1946–1966.
- 757 LaCasce, J. H., 2012: Surface quasigeostrophic solutions and baroclinic modes with expo-  
758 nential stratification. *Journal of Physical Oceanography*, **42** (4), 569–580, doi:10.1175/  
759 JPO-D-11-0111.1.
- 760 Lapeyre, G., 2009: What vertical mode does the altimeter reflect? On the decomposition  
761 in baroclinic modes and on a surface-trapped mode. *Journal of Physical Oceanography*,  
762 **39** (11), 2857—2874.
- 763 Lapeyre, G. and P. Klein, 2006: Dynamics of the upper oceanic layers in terms of surface  
764 quasigeostrophy theory. *Journal of Physical Oceanography*, **36** (2), 165–176.
- 765 Le Traon, P.-Y., 1990: Time scales of mesoscale variability and their relationship with  
766 space scales in the North Atlantic. *Journal of Marine Research*, **49** (3), 467–492, doi:  
767 10.1357/002224091784995828.
- 768 Le Traon, P.-Y., P. Klein, B. L. Hua, and G. Dibarboure, 2008: Do altimeter wavenumber  
769 spectra agree with the interior or surface quasigeostrophic theory? *Journal of Physical*  
770 *Oceanography*, **38**, 1137–1142.

771 Lin, X., J. Yang, D. Wu, and P. Zhai, 2008: Explaining the global distribution of peak-  
772 spectrum variability of sea surface height. *Geophysical Research Letters*, **35** (14), doi:  
773 10.1029/2008GL034312.

774 McWilliams, J. C. and G. R. Flierl, 1979: On the evolution of isolated, nonlinear vortices.  
775 *Journal of Physical Oceanography*, **9** (6), 1155–1182.

776 Menemenlis, D., J.-M. Campin, P. Heimbach, C. Hill, T. Lee, A. Nguyen, M. Schodlok,  
777 and H. Zhang, 2008: ECCO2: High resolution global ocean and sea ice data synthesis.  
778 *Mercator Ocean Quarterly Newsletter*, **31**, 13–21.

779 MODE Group, 1978: The mid-ocean dynamics experiment. *Deep-Sea Research*, **25** (10),  
780 859–910, doi:10.1016/0146-6291(78)90632-X.

781 Müller, P. and C. Frankignoul, 1981: Direct atmospheric forcing of geostrophic eddies. *Jour-*  
782 *nal of Physical Oceanography*, **11** (3), 287–308.

783 Müller, T. J. and G. Siedler, 1992: Multi-year current time series in the eastern North  
784 Atlantic Ocean. *Journal of Marine Research*, **50** (1), 63–98.

785 Philander, S. G. H., 1978: Forced oceanic waves. *Reviews of Geophysics*, **16** (1), 15–46.

786 Qiu, B., Bo, R. B. Scott, and S. Chen, 2008: Length scales of eddy generation and nonlinear  
787 evolution of the seasonally modulated South Pacific subtropical countercurrent. *Journal*  
788 *of Physical Oceanography*, **38** (7), 1515–1528, doi:10.1175/2007JPO3856.1.

789 Rhines, P. B. and F. P. Bretherton, 1973: Topographic Rossby waves in a rough-bottomed  
790 ocean. *Journal of Fluid Mechanics*, **61** (3), 583–607.

791 Roden, G., 2005: Shipboard acoustic doppler current profiling during cruise TT9306 (SAC  
792 ID 00016). Pangaea, doi:10.1594/PANGAEA.319488.

793 Samelson, R. M., 1992: Surface-intensified Rossby waves over rough topography. *Journal of*  
794 *Marine Research*, **50** (3), 367–384.

795 Scharffenberg, M. and D. Stammer, 2010: Seasonal variations of the large-scale geostrophic  
796 flow field and eddy kinetic energy inferred from the TOPEX/Poseidon and Jason-1 tandem  
797 mission data. *Journal of Geophysical Research*, **115**, C02 008, doi:10.1029/2008JC005242.

798 Scott, R. B., B. K. Arbic, E. P. Chassignet, A. C. Coward, M. Maltrud, A. Srivivasan, and  
799 A. Varghese, 2010: Total kinetic energy in three global eddy ocean circulation models  
800 and over 5000 current meter records. *Ocean Modelling*, **32** (3–4), 157–169.

801 Scott, R. B. and F. Wang, 2005: Direct evidence of an oceanic inverse kinetic energy cascade  
802 from satellite altimetry. *Journal of Physical Oceanography*, **35** (9), 1650–1666.

803 Stammer, D., 1997: Global characteristics of ocean variability estimated from regional  
804 TOPEX/POSEIDON altimeter measurements. *Journal of Physical Oceanography*, **27** (8),  
805 1743–1769, doi:10.1175/1520-0485(1997)027<1743:GCOOVE>2.0.CO;2.

806 Tailleux, R. and J. C. McWilliams, 2001: The effect of bottom pressure decoupling on the  
807 speed of extratropical, baroclinic Rossby waves. *Journal of Physical Oceanography*, **31** (6),  
808 1461–1476.

809 Taylor, G. I., 1921: Diffusion by continuous movements. *Proceedings of the London Mathe-*  
810 *matical Society*, **20**, 196–211.

811 Tulloch, R., J. Marshall, C. Hill, and K. S. Smith, 2011: Scales, growth rates and spectral  
812 fluxes of baroclinic instability in the ocean. *Journal of Physical Oceanography*, **41** (6),  
813 1057–1076.

814 Vanmarcke, E., 2010: *Random fields: analysis and synthesis*. World Scientific, Hackensack,  
815 NJ.

816 Vanneste, J., 2003: Nonlinear dynamics over rough topography: homogeneous and stratified  
817 quasi-geostrophic theory. *Journal of Fluid Mechanics*, **474**, 299–318.

- 818 Wang, D.-P., C. N. Flagg, K. Donohue, and H. T. Rossby, 2010: Wavenumber spectrum in the  
819 Gulf Stream from shipboard ADCP observations and comparison with altimetry measure-  
820 ments. *Journal of Physical Oceanography*, **40** (4), 840–844, doi:10.1175/2009JPO4330.1.
- 821 Wortham, C., 2013: A multi-dimensional spectral description of ocean variability with ap-  
822 plications. Ph.D. thesis, MIT/WHOI Joint Program, 184 pp.
- 823 Wunsch, C., 1997: The vertical partition of oceanic horizontal kinetic energy. *Journal of*  
824 *Physical Oceanography*, **27**, 1770–1794.
- 825 Wunsch, C., 1999: A summary of North Atlantic baroclinic variability. *Journal of Physical*  
826 *Oceanography*, **29** (12), 3161–3166, doi:10.1175/1520-0485(1999)029<3161:ASONAB>2.0.  
827 CO;2.
- 828 Wunsch, C., 2006: *Discrete Inverse and State Estimation Problems with Geophysical Fluid*  
829 *Applications*. Cambridge University Press.
- 830 Wunsch, C., 2008: Mass and volume transport variability in an eddy-filled ocean. *Nature*  
831 *Geoscience*, **1** (3), 165–168.
- 832 Wunsch, C., 2009: The oceanic variability spectrum and transport trends. *Atmosphere-*  
833 *Ocean*, **47** (4), 281–291.
- 834 Wunsch, C., 2010: Toward a mid-latitude ocean frequency-wavenumber spectral density and  
835 trend determination. *Journal of Physical Oceanography*, **40**, 2264–2281.
- 836 Wunsch, C. and D. Stammer, 1995: The global frequency-wavenumber spectrum of oceanic  
837 variability estimated from TOPEX/POSEIDON altimetric measurements. *Journal of Geo-*  
838 *physical Research*, **100** (C12), 24 895–24 910.
- 839 Xu, Y. and L.-L. Fu, 2012: The effects of altimeter instrument noise on the estimation of the  
840 wavenumber spectrum of sea surface height. *Journal of Physical Oceanography*, **42** (12),  
841 2229–2233, doi:10.1175/JPO-D-12-0106.1.

- 842 Zang, X., 2000: Spectral description of low frequency oceanic variability. Ph.D. thesis,  
843 MIT/WHOI Joint Program, 187 pp.
- 844 Zang, X. and C. Wunsch, 2001: Spectral description of low-frequency oceanic variability.  
845 *Journal of Physical Oceanography*, **31** (10), 3073–3095.
- 846 Zhai, X., H. L. Johnson, and D. P. Marshall, 2011: A model of Atlantic heat content and sea  
847 level change in response to thermohaline forcing. *Journal of Climate*, **24** (21), 5619–5632,  
848 doi:10.1175/JCLI-D-10-05007.1.



849 **List of Tables**

850     1     Statistics for comparison of the spectrum-model and the CMD. Instrument  
851            locations are shown in Fig. 12. Median  $D_\chi$  values represent the bias of the  
852            spectrum-model for  $EKE$  or  $\sigma_\theta$  within each depth bin. 41

TABLE 1. Statistics for comparison of the spectrum-model and the CMD. Instrument locations are shown in Fig. 12. Median  $D_\chi$  values represent the bias of the spectrum-model for  $EKE$  or  $\sigma_\theta$  within each depth bin.

Quantity	$EKE$	$\sigma_\theta$
# instruments	2179	1948
Correlation	0.85	0.77
Median $D_\chi$ , <700 m	-0.01	0.16
Median $D_\chi$ , 700–3000 m	-0.10	-0.11
Median $D_\chi$ , >3000 m	0.01	-0.45

## 853 List of Figures

- 854 1 Dominant phase speed (top left), period (top right), zonal wavelength (bot-  
855 tom left), and meridional wavelength (bottom right) based on the inverse  
856 of the first moment of the one-dimensional spectra. For zonal wavelength,  
857 the hatched area indicates regions where eastward propagation dominates;  
858 elsewhere, westward propagation dominates. For meridional wavelength, the  
859 hatched area indicates regions where poleward propagation dominates; else-  
860 where, equator ward propagation dominates. 45
- 861 2 Along-track wavenumber (left) and frequency (right) spectra from tracks span-  
862 ning 30°N to 40°N at the indicated longitude (solid line). Dashed lines show  
863 the spectrum-model at each location, discussed in section 4. Dotted lines  
864 show the spectra from AVISO gridded altimetry, interpolated along the satel-  
865 lite track. Vertical bars indicate the 95% confidence interval. 46
- 866 3 Observed (solid) and modeled (red dashed, discussed in section 4) frequency  
867 spectra of kinetic energy from moored instruments. All spectra are normalized  
868 by the total variance to compare the shapes. Vertical bars indicate the 95%  
869 confidence interval. 47
- 870 4 As in Fig. 3, but for the temperature spectrum. 48
- 871 5 Observed (solid) and modeled (dashed, discussed in section 4) wavenumber  
872 spectra of kinetic energy from shipboard ADCP. The transect spans 20°–30°N  
873 at 180°E at 100 m depth. The high wavenumber spectral slope for the model  
874 is  $k^{-2}$ . The vertical bar indicates the 95% confidence interval. 49

875	6	The spectrum-model (31) for SSH near 30°N, 190°E. Two-dimensional spectra	
876		$\Phi_\eta(k, \omega)$ (top left), $\Phi_\eta(l, \omega)$ (top right), and $\Phi_\eta(l, k)$ (bottom) are shown.	
877		Solid lines indicate the parameters in the model. One dimensional spectra	
878		are projected on a vertical plane, with high frequency/wavenumber power	
879		laws labeled. The nondispersive line, with phase speed $c_x$ , is most prominent	
880		in the $k$ - $\omega$ spectrum. Due to the difficulty of plotting positive and negative	
881		wavenumbers together on a logarithmic scale, we show the average of the	
882		positive and negative wavenumber half-spaces.	50
883	7	A 3D representation of the spectrum-model (31) for SSH near 30°N, 190°E.	
884		The red iso-surface illustrates the nondispersive line. Slices through the planes	
885		$\omega = 0$ , $l = 0$ , $k = 0$ , and $k = 6 \times 10^{-3}$ cpk are shown.	51
886	8	Global characteristics of the spectrum-model (31). Dominant zonal phase	
887		speed (top left), period (top right), zonal wavelength (bottom left), and merid-	
888		ional wavelength (bottom right) based on the first moment of the associated	
889		one-dimensional spectra.	52
890	9	Observed (solid) and modeled (dashed) frequency spectra of kinetic energy	
891		from moored instruments at 32°N, 232°E, 1481 m deep, as in Fig. 3, but now	
892		expanded to show the internal wave regime. The spectral peaks are at the	
893		inertial and $M_2$ tidal frequencies.	53
894	10	Observed (stars) and modeled (solid line) kinetic energy as a function of depth	
895		from moored instruments. Gray shading indicates EKE within a factor of 2	
896		of the spectrum-model prediction. Moorings are the same as those shown in	
897		Fig. 3 and 4.	54
898	11	As in Fig. 10 but showing the vertical structure of temperature variance. Gray	
899		shading indicates $\sigma_\theta$ within a factor of 2 of the spectrum-model prediction.	55
900	12	Locations of current meter mooring sites used.	56

901	13	Scatterplot of EKE (left) and $\sigma_\theta$ (right) from the spectrum-model and CMD instruments.	57
902			
903	14	The distribution of $D_{\text{EKE}}$ (left) and $D_{\sigma_\theta}$ (right) for three depth ranges: 0–700 m (blue), 700–3000 m (green) and below 3000 m (red).	58
904			
905	15	Autocorrelation function for temperature as a function of spatial (left) and temporal (right) separation based on the spectrum-model at 30°N, 190°E.	59
906			
907	16	Meridional velocity coherence as a function of meridional separation at 30°N, 190°E.	60
908			
909	17	Horizontally variable part of (A3) for $\tilde{p}$ , $\tilde{\rho}$ , $\tilde{\zeta}$ , $\tilde{\theta}$ (top left), $\tilde{u}$ (top right), $\tilde{v}$ (bottom left), and $\tilde{w}$ (bottom right).	61
910			
911	18	Vertical structure part of (A3) for $\tilde{\theta}$ at 39°N, 230°E. Multiplying by the horizontally variable part shown in Fig. 17 gives the temperature variance.	62
912			

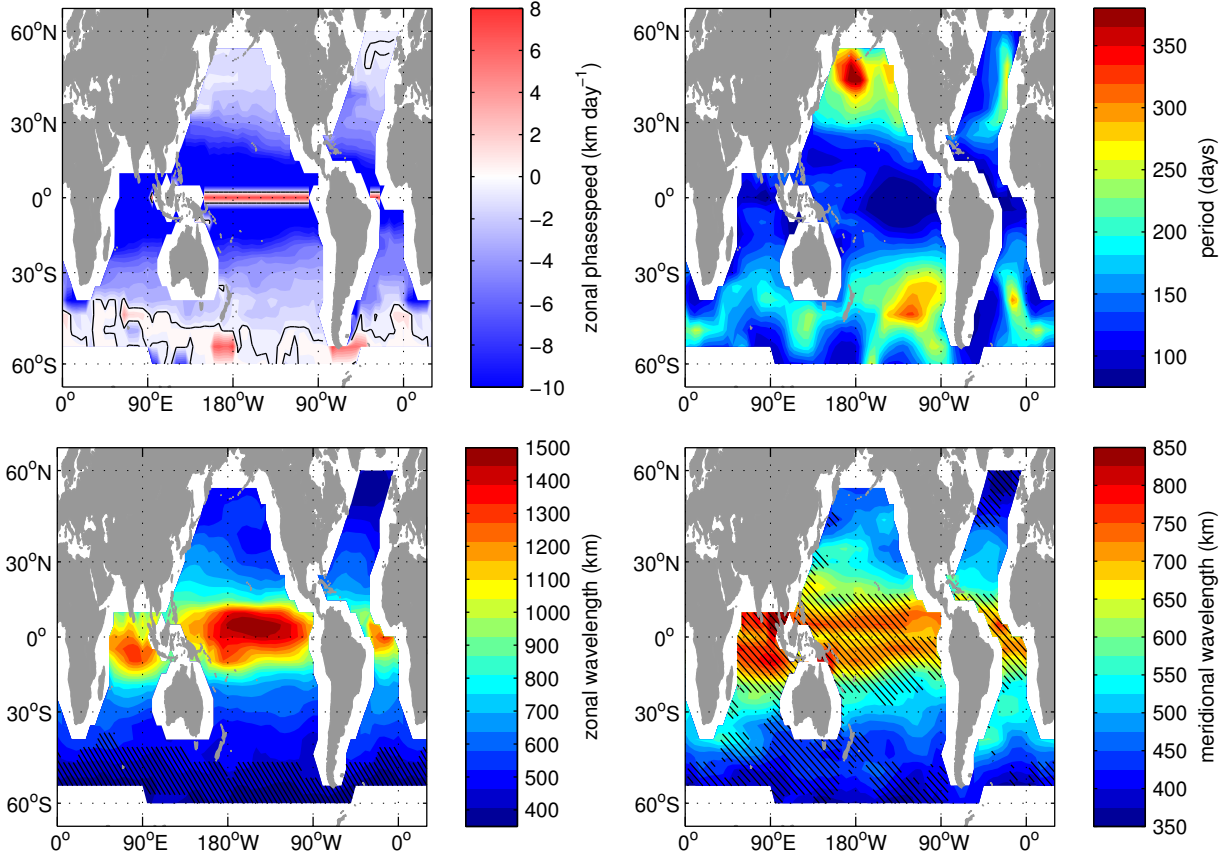


FIG. 1. Dominant phase speed (top left), period (top right), zonal wavelength (bottom left), and meridional wavelength (bottom right) based on the inverse of the first moment of the one-dimensional spectra. For zonal wavelength, the hatched area indicates regions where eastward propagation dominates; elsewhere, westward propagation dominates. For meridional wavelength, the hatched area indicates regions where poleward propagation dominates; elsewhere, equator ward propagation dominates.

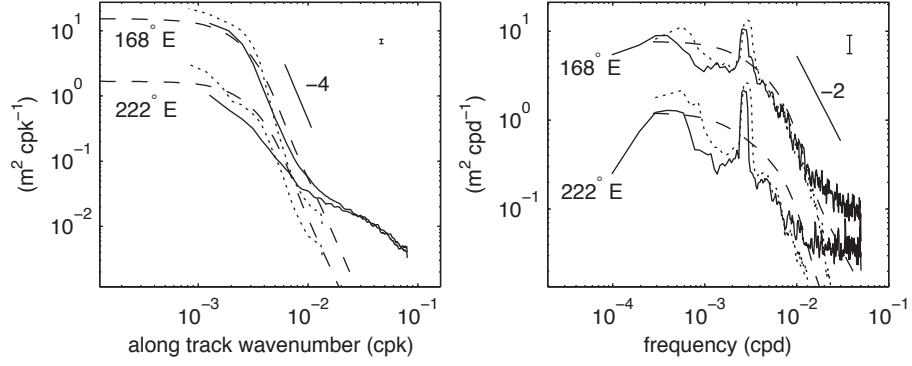


FIG. 2. Along-track wavenumber (left) and frequency (right) spectra from tracks spanning  $30^\circ N$  to  $40^\circ N$  at the indicated longitude (solid line). Dashed lines show the spectrum-model at each location, discussed in section 4. Dotted lines show the spectra from AVISO gridded altimetry, interpolated along the satellite track. Vertical bars indicate the 95% confidence interval.

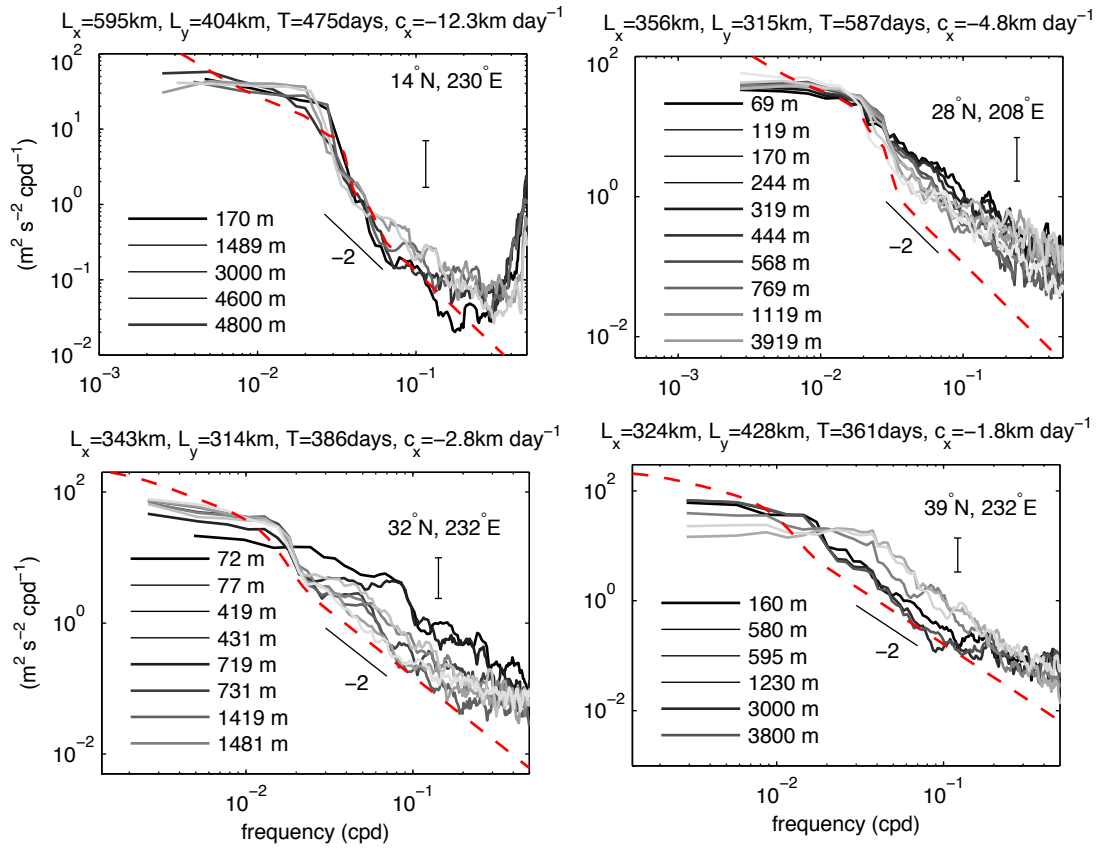


FIG. 3. Observed (solid) and modeled (red dashed, discussed in section 4) frequency spectra of kinetic energy from moored instruments. All spectra are normalized by the total variance to compare the shapes. Vertical bars indicate the 95% confidence interval.



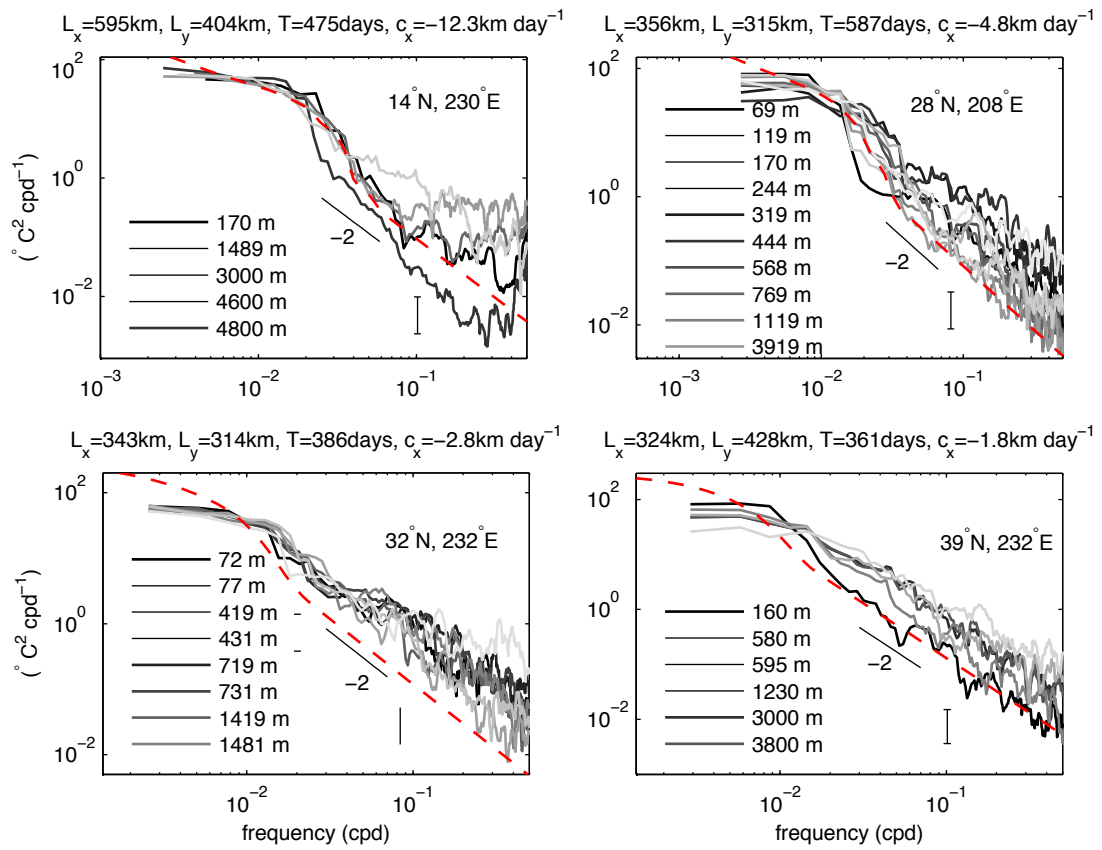


FIG. 4. As in Fig. 3, but for the temperature spectrum.

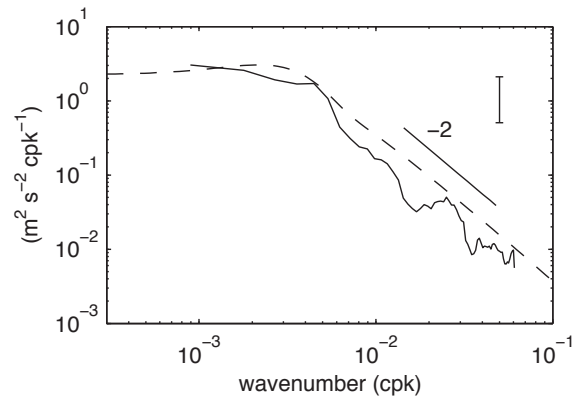


FIG. 5. Observed (solid) and modeled (dashed, discussed in section 4) wavenumber spectra of kinetic energy from shipboard ADCP. The transect spans  $20^{\circ}$ – $30^{\circ}$ N at  $180^{\circ}$ E at 100 m depth. The high wavenumber spectral slope for the model is  $k^{-2}$ . The vertical bar indicates the 95% confidence interval.

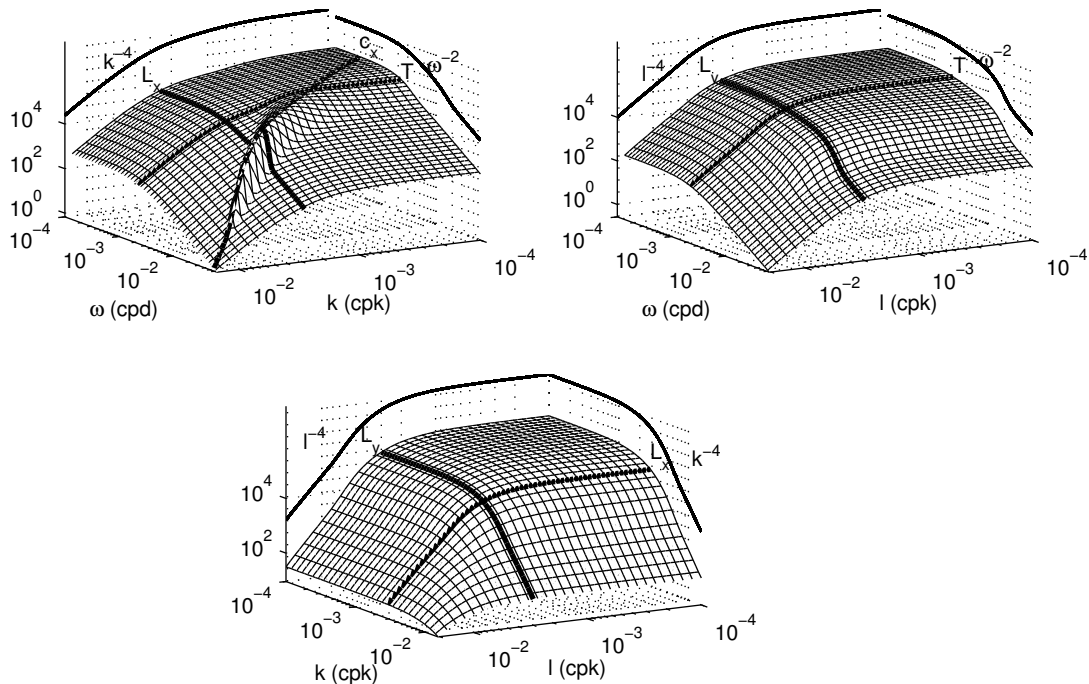


FIG. 6. The spectrum-model (31) for SSH near  $30^\circ\text{N}$ ,  $190^\circ\text{E}$ . Two-dimensional spectra  $\Phi_\eta(k, \omega)$  (top left),  $\Phi_\eta(l, \omega)$  (top right), and  $\Phi_\eta(l, k)$  (bottom) are shown. Solid lines indicate the parameters in the model. One dimensional spectra are projected on a vertical plane, with high frequency/wavenumber power laws labeled. The nondispersive line, with phase speed  $c_x$ , is most prominent in the  $k$ - $\omega$  spectrum. Due to the difficulty of plotting positive and negative wavenumbers together on a logarithmic scale, we show the average of the positive and negative wavenumber half-spaces.

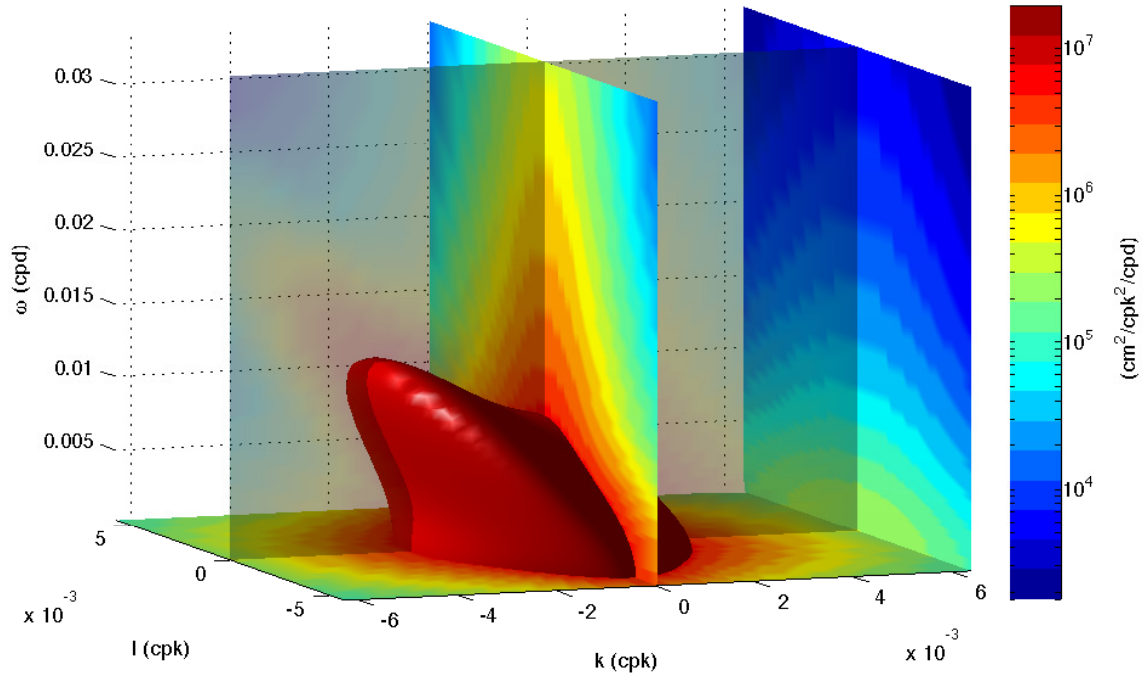


FIG. 7. A 3D representation of the spectrum-model (31) for SSH near 30°N, 190°E. The red iso-surface illustrates the nondispersive line. Slices through the planes  $\omega = 0$ ,  $l = 0$ ,  $k = 0$ , and  $k = 6 \times 10^{-3}$  cpk are shown.

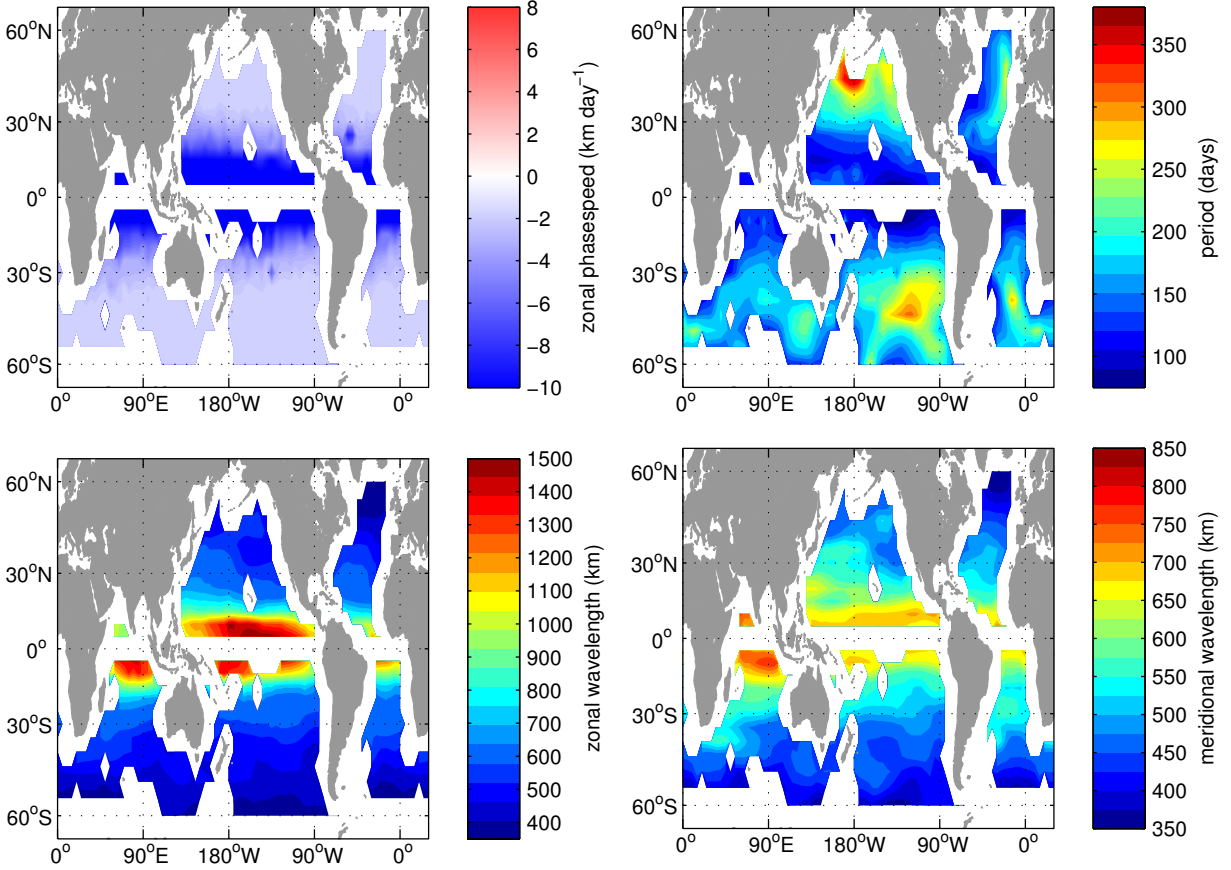


FIG. 8. Global characteristics of the spectrum-model (31). Dominant zonal phase speed (top left), period (top right), zonal wavelength (bottom left), and meridional wavelength (bottom right) based on the first moment of the associated one-dimensional spectra.

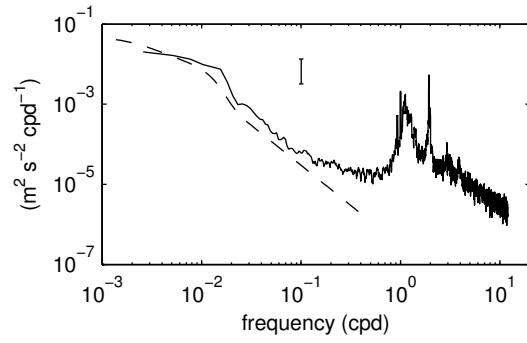


FIG. 9. Observed (solid) and modeled (dashed) frequency spectra of kinetic energy from moored instruments at  $32^{\circ}\text{N}$ ,  $232^{\circ}\text{E}$ , 1481 m deep, as in Fig. 3, but now expanded to show the internal wave regime. The spectral peaks are at the inertial and  $M_2$  tidal frequencies.

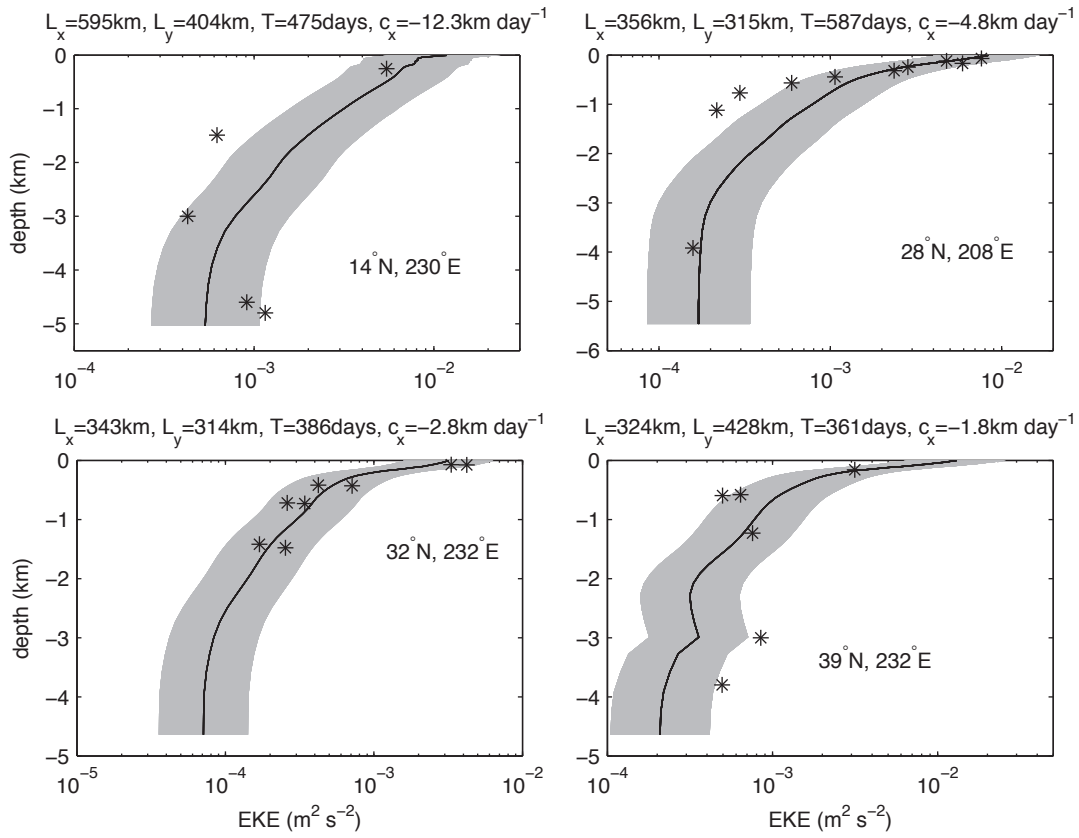


FIG. 10. Observed (stars) and modeled (solid line) kinetic energy as a function of depth from moored instruments. Gray shading indicates EKE within a factor of 2 of the spectrum-model prediction. Moorings are the same as those shown in Fig. 3 and 4.

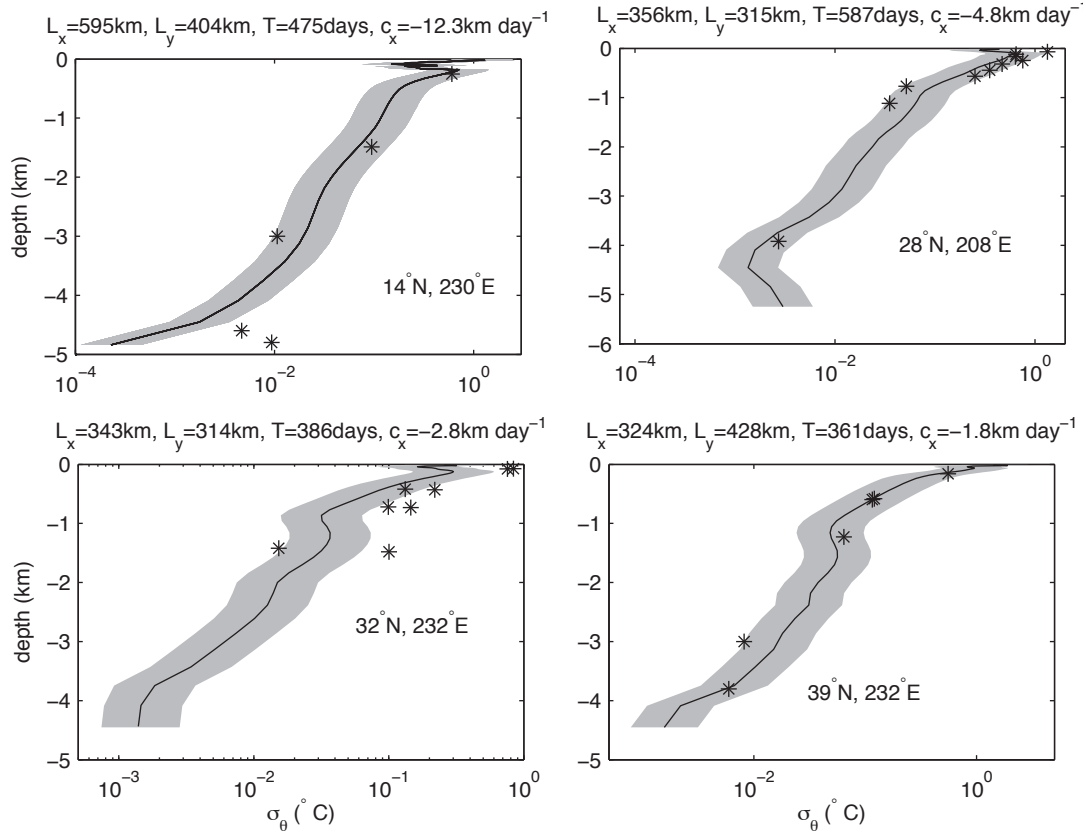


FIG. 11. As in Fig. 10 but showing the vertical structure of temperature variance. Gray shading indicates  $\sigma_\theta$  within a factor of 2 of the spectrum-model prediction.



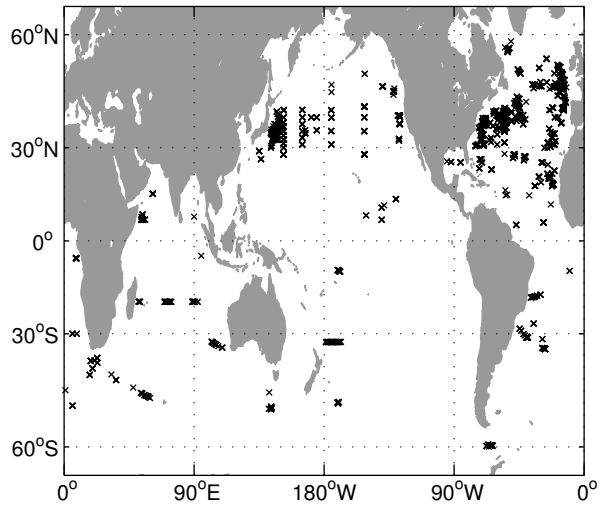


FIG. 12. Locations of current meter mooring sites used.

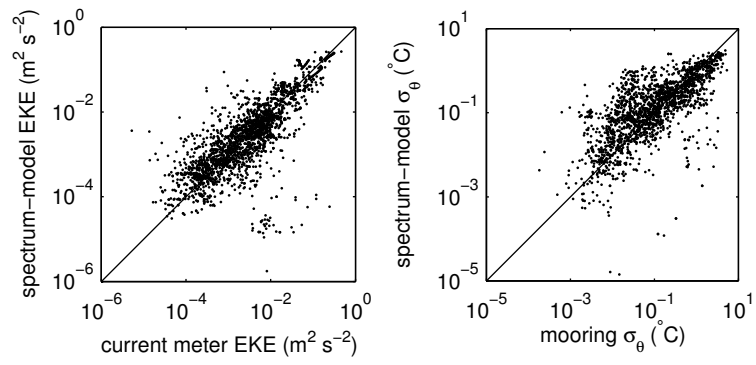


FIG. 13. Scatterplot of EKE (left) and  $\sigma_\theta$  (right) from the spectrum-model and CMD instruments.

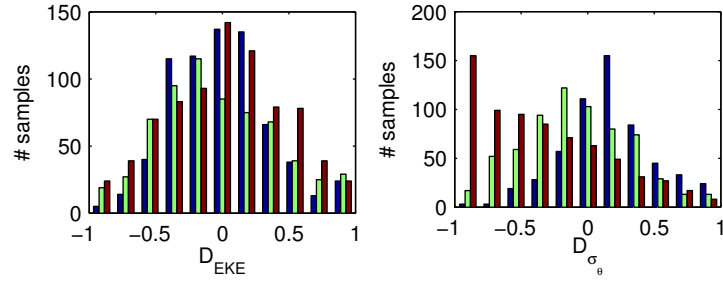


FIG. 14. The distribution of  $D_{EKE}$  (left) and  $D_{\sigma_\theta}$  (right) for three depth ranges: 0–700 m (blue), 700–3000 m (green) and below 3000 m (red).

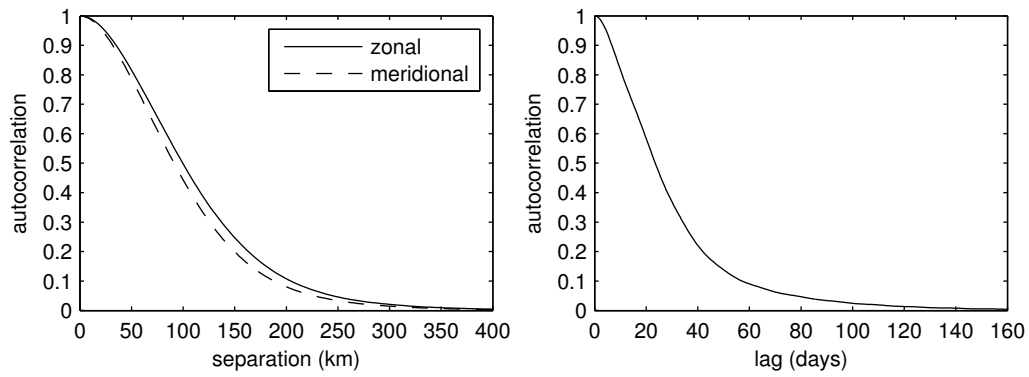


FIG. 15. Autocorrelation function for temperature as a function of spatial (left) and temporal (right) separation based on the spectrum-model at  $30^{\circ}\text{N}$ ,  $190^{\circ}\text{E}$ .

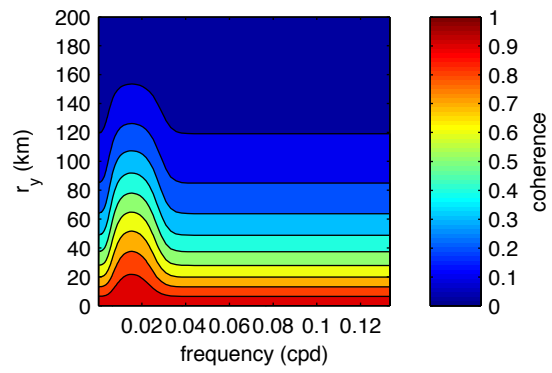


FIG. 16. Meridional velocity coherence as a function of meridional separation at  $30^\circ\text{N}$ ,  $190^\circ\text{E}$ .

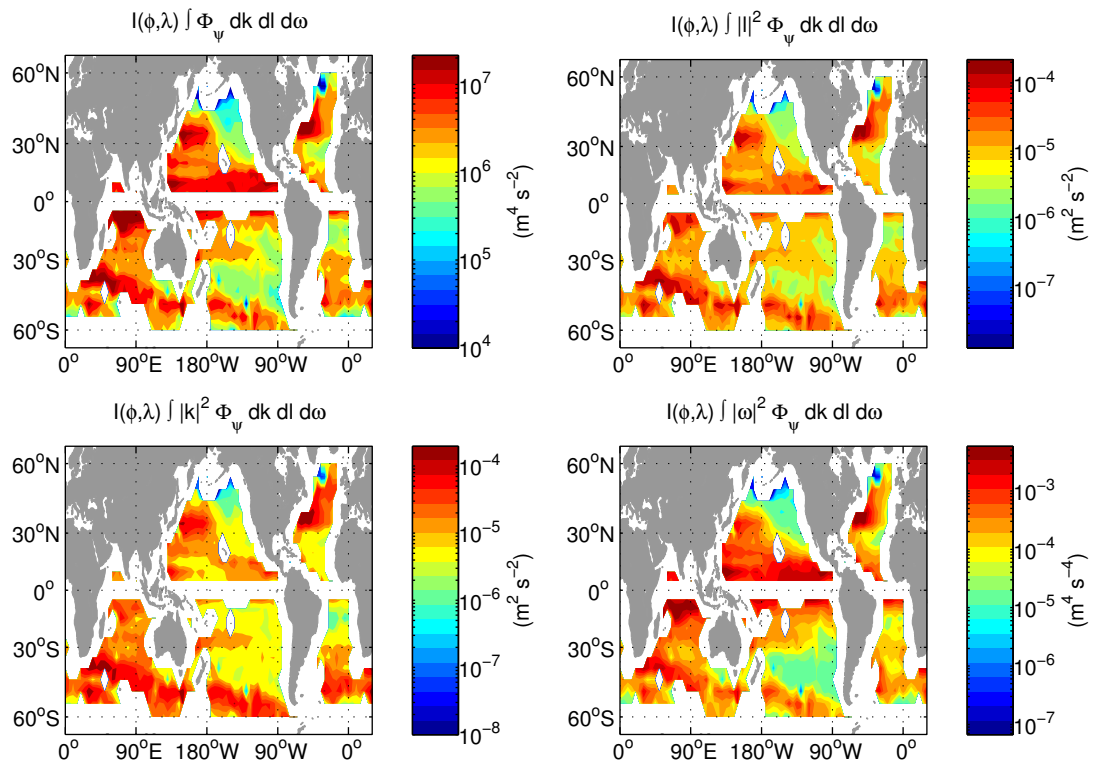


FIG. 17. Horizontally variable part of (A3) for  $\tilde{p}$ ,  $\tilde{\rho}$ ,  $\tilde{\zeta}$ ,  $\tilde{\theta}$  (top left),  $\tilde{u}$  (top right),  $\tilde{v}$  (bottom left), and  $\tilde{w}$  (bottom right).

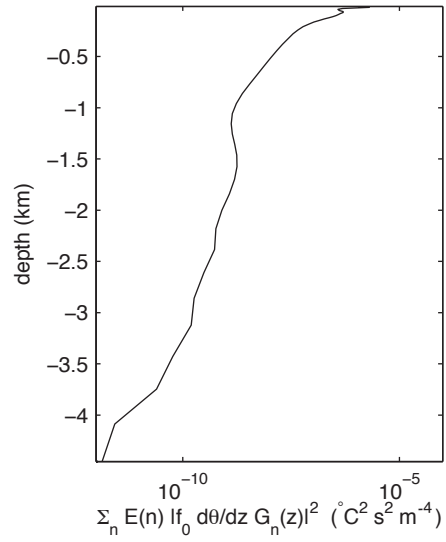


FIG. 18. Vertical structure part of (A3) for  $\tilde{\theta}$  at  $39^\circ\text{N}$ ,  $230^\circ\text{E}$ . Multiplying by the horizontally variable part shown in Fig. 17 gives the temperature variance.